Summer 8-12-2022

Additively Manufactured Polymer and Metal Lattice Structures with Eulerian Path

Adeeb Ibne Alam
adeeb.alam@maine.edu

ADDITIVELY MANUFACTURED POLYMER AND METAL LATTICE STRUCTURES WITH EULERIAN PATH

By

Adeeb Ibne Alam

B.Sc. Bangladesh University of Engineering and Technology, 2017

A THESIS

Submitted in Partial Fulfillment of the

Requirements for the Degree of

Master of Science

(In Mechanical Engineering)

The Graduate School

The University of Maine

August 2022

Advisory Committee:

Bashir Khoda, Assistant Professor of Mechanical Engineering, Advisor

Masoud Rais-Rohani, Professor & Chair of Mechanical Engineering

Keith Berube, Associate Professor, Mechanical Engineering Technology

ADDITIVELY MANUFACTURED POLYMER AND METAL LATTICE STRUCTURES WITH EULERIAN PATH

By Adeeb Ibne Alam

Thesis Advisor: Dr. Bashir Khoda

An Abstract of the THESIS Presented
in Partial Fulfillment of the Requirements for the
Degree of Master of Science
(In Mechanical Engineering)
August 2022

Lattice structure manufacturing with polymers and metals can benefit from the use of Eulerian paths. In this research, two types of lattice fabrication methods are studied where the Eulerian path can be applicable. Polymer lattice is improved by using a new assembly design, while a new way of metal lattice fabrication is discussed.

For the fused filament fabrication process, a new interlocking design and assemble-based lattice structure building approach is investigated by increasing continuity in layers and avoiding support structures. To minimize contour plurality, Eulerian paths between the edges were enforced. Two configurations in the form of cubic and octet lattice structures are examined. The compressive performance of the designed lattice structures is compared with the traditional single-build direct 3D printed lattice structures. The mechanical performance (e.g., peak stress, specific energy absorption) of the assembled structures is found to be generally better than their direct print counterparts. The empirical constants of the Ashby-Gibson power law are found to be larger than their suggested values in both direct print and assembly techniques. However, their values are more compliant for octet assembled structures, which are less susceptible to manufacturing imperfections.

A novel method of metal lattice manufacturing is introduced where a straight wire is bent to make intermediate structures, they are stacked, and loose nodes are joined to get the final lattice. The limitations of this method are studied, and a machine is constructed that can overcome some of the limitations and produce fabricable and stackable structures. These structures, generated by a custom-made visual basic code, can be periodic or aperiodic using a function to optimize the topology. The transient liquid phase (TLP) diffusion bonding method is studied as an appropriate joining method due to the inaccessibility of the nodes after stacking.

TABLE OF CONTENTS

LIST OF TABLES

LIST OF FIGURES

CHAPTER 1: INTRODUCTION

Lattice structures, a class of cellular solids, consist of repetitive connected members or tessellated unit cells with multiple struts that are connected through end-point contacts or nodes [1]. Periodically assembling these unit cells forms a complex structural network [2], which can be a bending- or stretch-dominated structure that follows Maxwell's criterion [3].

These low-density structures have the potential to demonstrate higher performance than monolithic structures and are often better suited for applications in mechanical, phononic, thermal, and biological fields [4], [5]. Furthermore, compared to stochastic cellular structures (i.e., irregular foams), the mechanical properties of the periodic cellular structures are more predictable and often exhibit superior performance and multi-functional properties [6] due to their well-ordered geometries [7], [8].

The superior performance expected from a lattice structure depends on proper design parameters (cell dimension) and manufacturing accuracy (overall porosity and properly connected nodes) [9]. However, the far extents of 3D cellular architecture are often unaffordable due to design and manufacturing limitations [10]. Fabrication imperfections, i.e., topological (variations in nodal connectivity and missing struts) and dimensional (variations in cellular dimensions) [11], are common in lattice structures due to the multi-stage complex manufacturing process [1], and can cause significant degradation in their intended performance, e.g., elastic moduli and compressive yield strength [10], [12], [13].

Due to complicated architecture and nodal connectivity, the traditional lattice manufacturing processes available today are not economical. Most of the manufacturing techniques of lattices are

additive based. Some of the most commonly used lattice structure manufacturing techniques are interlocked modular design, electroless nickel plating, robocasting, high-temperature forming, wire woven, investment casting, etc. [14]–[18]. 3D printing techniques like fused filament fabrication (FFF) for polymers, as well as selective laser melting (SLM), and electron beam melting (EBM) for metals are some of the popular lattice manufacturing methods [19]–[22].

However, these manufacturing processes face challenges like material entrapment, the limited scope of printable material, uncontrolled microstructure, contour plurality, and staircase effect, which significantly reduce a lattice's mechanical properties [23]. Contour plurality is the concept of having multiple discrete contours in a single layer of the material deposition-based 3D printing process. Studies have shown continuity in the material deposition in 3D printing can result in higher overall structural strength [24], [25]. Multiple discrete contours can intertwine more manufacturing defects to the 3D printed structures.

To resolve some of the issues with manufacturing lattice structures using the 3D printing process, an eighteenth-century concept of the Eulerian path (or, Eulerian trail) is incorporated into this thesis. This term is fundamental to graph theory. If we consider a collection of points which are connected with some collection of paths, where paths are noted as edges and points are noted as nodes, an Eulerian path is a trail that follows every edge only once allowing revisiting to the nodes. This concept can be synonymously applied to the material deposition toolpath for a lattice manufacturing. Each route of the toolpath can be considered an edge, and each corner of the lattice can be considered a node. The contour plurality can be significantly reduced if the deposition toolpath follows the Eulerian path, which is the most continuous path possible between two nodes. The Eulerian path and its application in 3D printing and lattice manufacturing by wire bending are discussed in Chapters 2 and 3, respectively.

The remaining portion of the thesis is organized as follows:

Chapter 2 is the study of lattices using Fused Filament Fabrication (FFF), also known as FDM (Fused Deposition Modeling). In addition, a new type of lattice manufacturing method of assembling separately printed strut structures is presented. Part of this chapter has already been published in the journal of "3D Printing and Additive Manufacturing".

Chapter 3 focuses on the possibility and manufacturability of a metal lattice manufacturing process using continuous metal rods bent at certain places; several parts are stacked, dipped, and joined to form the final structure.

CHAPTER 2 : MECHANICAL PERFORMANCE OF 3D PRINTED POLYMER LATTICE STRUCTURES: ASSEMBLED VS. DIRECT PRINT

2.1 Introduction

3D printing or additive manufacturing (AM) relies on the incremental deposition of one or two-dimensional forms of raw materials, such as polymer or metal, to form a three-dimensional object. AM can be used to fabricate complicated geometries, including lattice structures. However, 3D printed lattice structures are prone to deficiencies in mechanical performance, functionality, and feasibility caused by anisotropy, insufficient interlayer adhesion, microvoids or uncontrolled porosity, staircase effect, uneven surfaces, overhang support, shrinkage, and required resources [1], [26], [27]. Cellular structures have voids designed within them by the tessellated pattern used. During slicing of the object into layers, the process can generate numerous disconnected features, which are defined as contour plurality [26]–[29]. The presence of contour plurality exemplifies the lack of performance by discontinuous and interrupted path plans, which can cause reduced structural integrity, surface roughness, anisotropy, and weaker interlayer adhesion [26], [30]–[32].

A large body of research exists in the literature aimed at comparing the characteristics and performance of lattice structures that are fabricated with extrusion-based processes. Higher compressive strength in Kagome lattice structures is reported along the print orientation and the smoother 3D printed surface [30]. Building a cellular structure in a layer-based AM usually requires a support structure. Increasing the cell's complexity or reducing its size will introduce trapped or difficult-to-remove support structures, another limitation for direct print lattice structures with an extrusion-based AM process [31].

This chapter is published in the journal of “3D Printing and Additive Manufacturing” under the name “Mechanical Performance of 3D Printed Lattice Structures: Assembled vs. Direct Print.” Except for section 2.2.2.

Dong et al. [32] studied the significance of process parameters and build direction in extrusion-based printing of lattice structures. They used the Taguchi method to optimize the process parameters for improved print quality and mechanical performance. Three non-stochastic lattice structures (BCC, BCC-Z, and 4+1 vertical strut pattern) were printed with PLA material, and their shear and bending strengths were experimentally investigated [33]. They found that the 3D printed lattice structures behaved well under high-shear and out-of-plane compressive load applications.

The mechanical performance of lattice structures is often predicted by using the Gibson-Ashby equation, which is expressed with a quadratic or higher-order scaling relationship between strength, modulus, and relative density. However, due to the fabrication imperfections discussed previously, the performance behavior of a 3D printed lattice may not follow the empirical constant of the power law. To address this shortcoming, post-processing of 3D printed lattice structures (e.g., annealing) has been proposed for amorphous and semi-crystalline composites [34]. A recent attempt to delineate fundamental linkages between volumetric porosity, surface roughness defects, and the resulting performance of lattice structures was reported by Jiang et al. [35], where they used principal component analysis to determine the elastic strain fields variation and develop an exponential degradation factor in the Gibson-Ashby equation.

In light of the challenges associated with direct 3D printing of lattice structures and informed by the prior works reported in the literature, a comprehensive study of lattice fabrication techniques is conducted, and their performance is analyzed for extrusion-based processes. The pre-processing knowledge base of extrusion-based 3D printing is compiled and contemplated with post-processing performance measurement for lattice structure printing. The effect of contour plurality on mechanical performance is investigated. To reduce contour plurality, a continuous filament deposition-based design is proposed that requires the assembly of the separately printed parts for

constructing lattice structures. Both cubic and octet lattice structures are printed using the assembly technique. Their mechanical performance at different length scales is measured and compared with the traditional direct print structures of similar patterns. The results from the compression tests are compared with existing analytical models for comparison.

2.2 Methodology

2.2.1 Design philosophy and printing of lattice structures

3D printing process parameters such as filament deposition direction and build direction can affect the mechanical performance of 3D printed lattices. Rajpurohit et al. [24] showed that raster angle can be a defining factor for the tensile strength of a 3D printed part. Parts made with a 0° raster angle (load along the filament deposition) exhibited the highest tensile strength compared to all other raster angles. Kiendl et al. [36] also obtained similar results with 0° raster layup having the highest tensile strength.

Based on their deformation behaviors, cellular solids are categorized into bending- and stretch-dominated structures. The bending-dominated structures typically show one or more degrees of freedom, often with sparse strut nodal connectivity. As nodal connectivity is increased, the nodes (joints) become more rigid, causing higher stiffness with struts experiencing mainly tension or compression depending upon their alignment, hence, leading to stretch-dominated structures [6], [37].

A set of strut assemblies, the building elements of 3D structures, are designed with an interlocking mechanism, as shown in Figure 2-1. The macro struts are printed separately on the print bed along a continuous toolpath with nearly zero support material. The relative density of both printed lattices (cubic and octet) is kept between 6% to 16% by changing the strut length from 14 mm to 24 mm

for cubic cells and from 9.9 mm to 17 mm for octet cells. To ensure successful material deposition in each layer during direct lattice print, the cross-sectional dimensions of the struts are kept at 2 mm x 2 mm for the cubic unit cell and 1.4 mm x 1.4 mm for the octet unit cell. Below these dimensions, the continuity of extruded material becomes highly irregular. Similarly, above a 24 mm cubic cell size, the bridging method to print filament without support becomes insufficient, and delamination is observed in the overhanging strut. The octet lattice's strut angle is maintained at 45º due to its support-free extrudability.

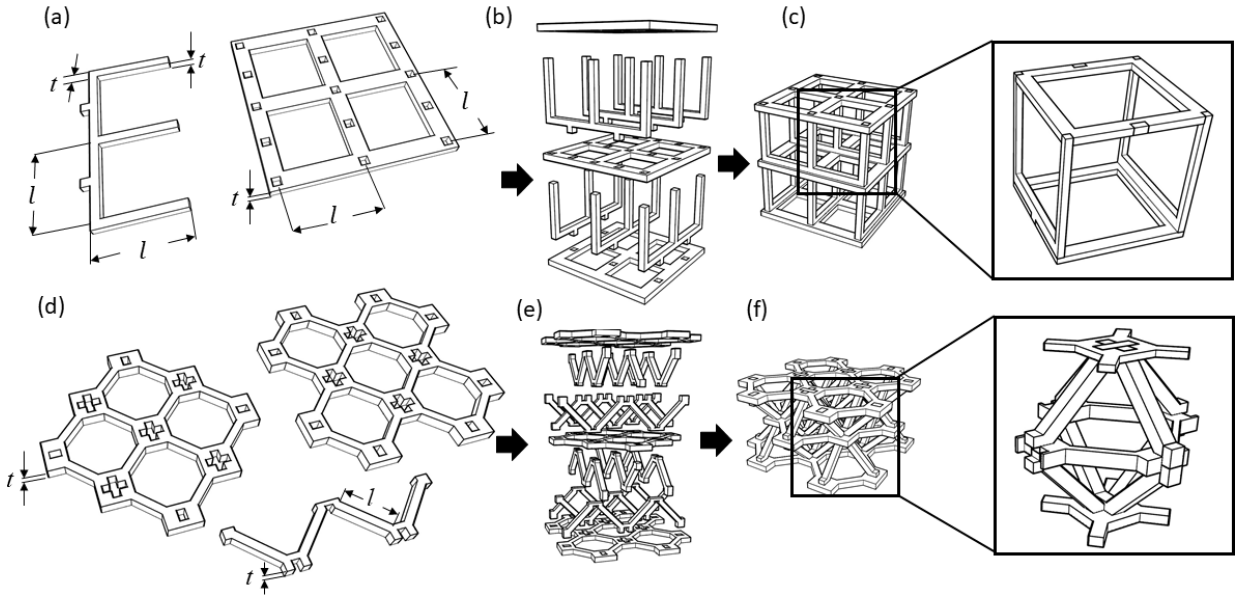

Figure 2-1: Design of Assembly-based lattice structures, (a) Unit strut sub-assembly and baseplate definition for a cubic lattice, (b) assembly method for 2x2x2 cell size cubic lattice, (c) fully assembled and unit cell for cubic lattice, (d) unit strut sub-assembly and baseplates definition for 2x2x1 cell size octet lattice, (e) assembly method for 2x2x1 cell size octet lattice, and (f) fully assembled and unit cell for octet lattice.

2.2.2 Implication of Eulerian path on designing strut sub-assembly

Both types of lattice structures (cubic as bending dominated and octet as stretch dominated) are designed in this work to demonstrate the effect of the continuous deposition of materials. To decrease contour plurality and increase continuity in the material deposition path the design was done with the concept of Eulerian path in mind. If we look at the design of cubic strut sub-assembly, we can see that a strut can be constructed with continuous toolpath along the strut length like Figure 2-2(c), with a mixture of continuous toolpath along the strut length and a zig-zag toolpath like Figure 2-2(d), or completely zig-zag toolpath like Figure 2-2(e). According to the previous studies [24], [36] continuous toolpath (Figure 2-2(c)) is the most desirable option for ensuring higher mechanical properties. To confirm the toolpath continuity, the concept of Euler path can be employed in the design.

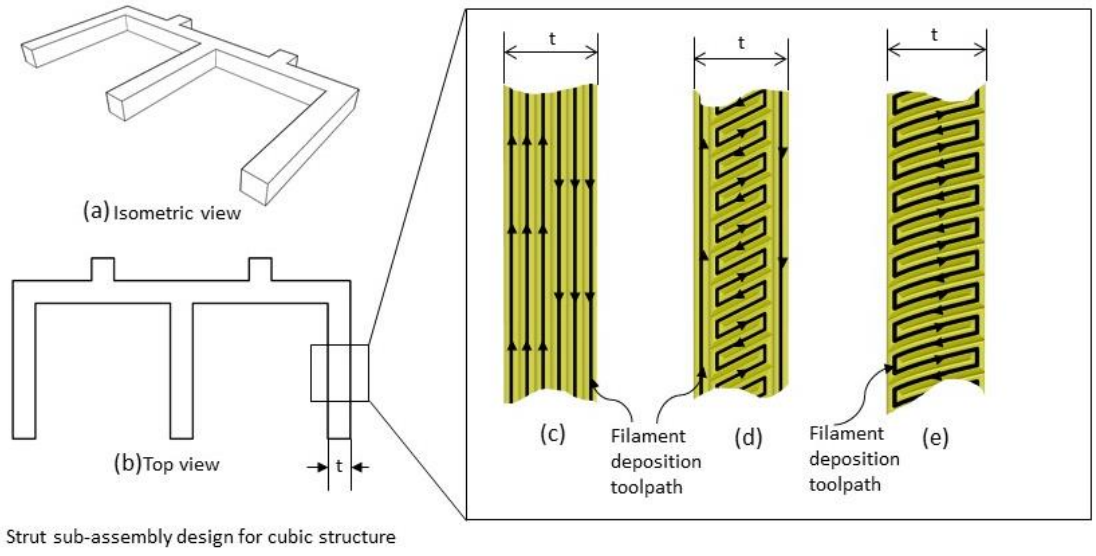

Figure 2-2: Possibilities of filament deposition toolpath on a cubic strut sub-assembly, (a) and (b) isometric and top view of the cubic strut sub-assembly design, (c) continuous, (d) mixed, and (e) zig-zag toolpath along the strut length.

The Eulerian path or Euler path and its associated terms (Eulerian Circuit, Hamiltonian Path, and Hamiltonian Circuit) are the fundamental concepts of graph theory. The terminologies utilized in this research are described below [38]:

Graph: a graph is a set of objects where some objects are related to each other in pairs.

Node: An object in the graph is considered a point or node.

Vertex/Edge: The connection between two nodes is an edge.

Eulerian path: A path that uses every edge in a graph only once, visiting all the nodes (nodes can be visited multiple times)

Eulerian circuit: If an Eulerian path starts and ends at the same node, it is called an Eulerian circuit.

Hamiltonian path: Hamiltonian path uses each node only once, and does not need to use all the edges.

Hamiltonian circuit: If a Hamiltonian path starts and ends at the same node, it is called a Hamiltonian circuit.

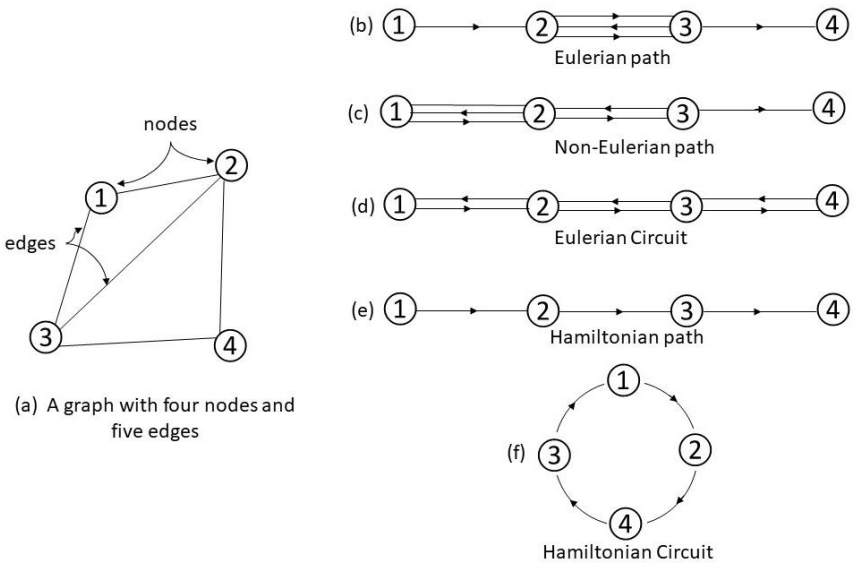

Figure 2-3: Terminologies of graph theory, (a) graph, nodes, and edges, (b) Eulerian path, (c) Non-Eulerian path, (d) Eulerian circuit, (e) Hamiltonian path, (f) Hamiltonian circuit.

A deposition toolpath that follows an Eulerian circuit is the most continuous path possible for the toolpath. If one layer of the material deposition's toolpath can be constructed as an Eulerian circuit, the whole layer can be printed without any obstacle. The necessary condition for an Eulerian circuit in a graph of toolpath for each node (in this case, the nodes of the lattices eventually represent the node of the graph, too) to have vertices (in this case, struts of the lattices) with an even number of degree. In other words, each neighboring nodes should relate to each other in such a way that the toolpath can go to and from a neighboring node, which makes a pair. If the toolpath is made with these sets of toolpath pairs, the toolpath can be continuous and need not be disrupted, creating an unbroken contour.

Both the strut sub-assembly of cubic and octet lattices can be divided into two equal and separate parts between each node pair, as shown in Figures 2-4 and 2-5. If we consider each corner of the sub-assembly as one node, the design consists of each node connected to the neighboring node

with two paths. So, the material deposition nozzle can take one path to go forward and another path to go backward and hence complete the Eulerian circuit.

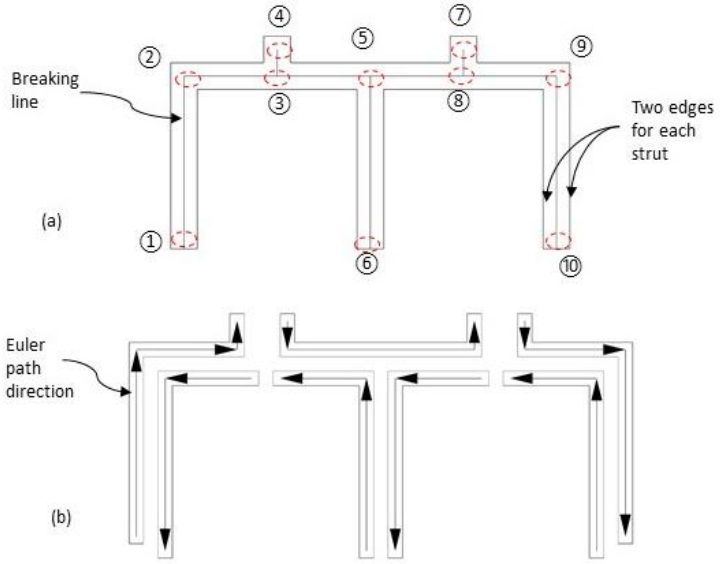

Figure 2-4: Designing cubic strut sub-assembly that follows the Eulerian path completing the Eulerian circuit, (a) dividing each path between the nodes in strut sub-assembly, (b) Eulerian path followed by the material deposition toolpath.

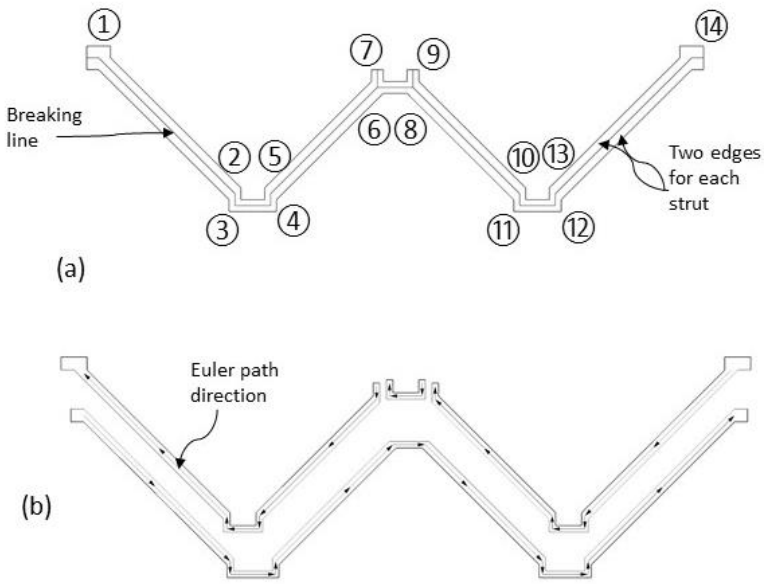

Figure 2-5: Designing octet strut sub-assembly that follows the Eulerian path Eulerian circuit, (a) dividing each path between the nodes in strut sub-assembly, (b) Eulerian path followed by the material deposition toolpath.

2.2.3 Printing parameters and processes

An extrusion-based 3D printer (Ender 3) was used to print the polymer lattice structures in this study. All samples were printed using Polylactic Acid (PLA) material, with a nozzle size of 0.4 mm, nozzle temperature of 205°C, and bed temperature of 70°C. The digital models of the octet and cubic lattices were created in Rhino 6. Lattice structures after assembly are shown in Figure 2-6. The strut assemblies were printed flat on the 3D printer bed and joined using cyanoacrylate-based adhesive (GlueMasters), which takes less than 2 minutes. The direct print lattice structures were printed following the bridging method for the overhanging horizontal struts. The total build times and the time saving between the cubic and octet structures using direct print and assembly manufacturing are listed in Table 2-1. Efforts were made during the design phase to minimize variation in the unit cell parameters (i.e., relative density, cell size, strut dimensions) to ensure

consistency between the structure type. However, a slight variation can be observed (as shown in Table 2-2) due to design, extrusion, and assembly limitations. For each density of four types of lattices studied one specimen was manufactured for compressive test.

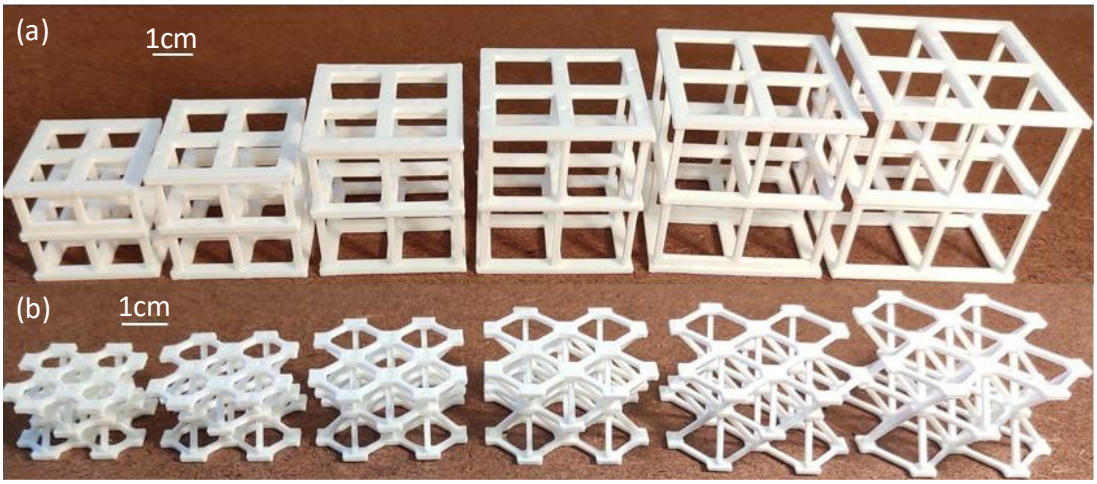

Figure 2-6: Lattices designed and manufactured by the assembly method with different lattice densities. (a) Cubic lattices (2x2x2) and (b) Octet lattices (2x2x1).

Table 2-1: Print time for cubic and octet lattices.

Lattice type	**Cell dimension**	**Strut length, l (mm)**	**Print time for direct print lattice (min)**	**Print time for assembled lattice (min)**	**Time Saving (%)**
Cubic	2x2x2	14	34	21	38
		16	39	24	38
		18	49	29	40
		20	54	31	42
		22	59	34	42
		24	68	36	47
Octet	2x2x1	9.9	22	13	40
		11.31	26	15	42
		12.73	31	17	45
		14.14	35	18	48
		15.56	40	19	52
		16.97	44	21	52

2.3 Results and discussion

The direct print and assembled lattice samples were tested under out-of-plane quasi-static compression using an MTS Criterion universal testing machine with a 50-kN load cell at a 10-Hz data acquisition rate and a 5-mm/min crosshead speed. Stress values were calculated as the measured applied compressive force divided by the surface area of the lattice at each loading increment, whereas the ratios of the corresponding crosshead displacements to the initial distance between the loading heads were used to calculate the non-dimensional displacements, commonly used strain like responses for lattice structures [6], [39].

The compressive stress-strain curves of the cubic direct print lattice structures are shown in Figure 2-7(a). Depending on the strut thickness-to-length ratio, t/l, as defined in Figure 2-1, peak stress varies from the minimum of 0.2 MPa for $t/l = 0.08$ to the maximum of 2.0 MPa for $t/l = 0.14$, with max strain reaching 0.022. If the curves were associated with a fully solid material, the transition point at peak stress would correspond to the onset of inelastic response and plastic deformation. However, for lattice structures, the transition point can be caused by different mechanisms, such as plastic deformation, lateral instability, or a combination of instability of the struts under axial compression and plastic deformation, with the latter being more confined to the highest-stress locations in the joint regions.

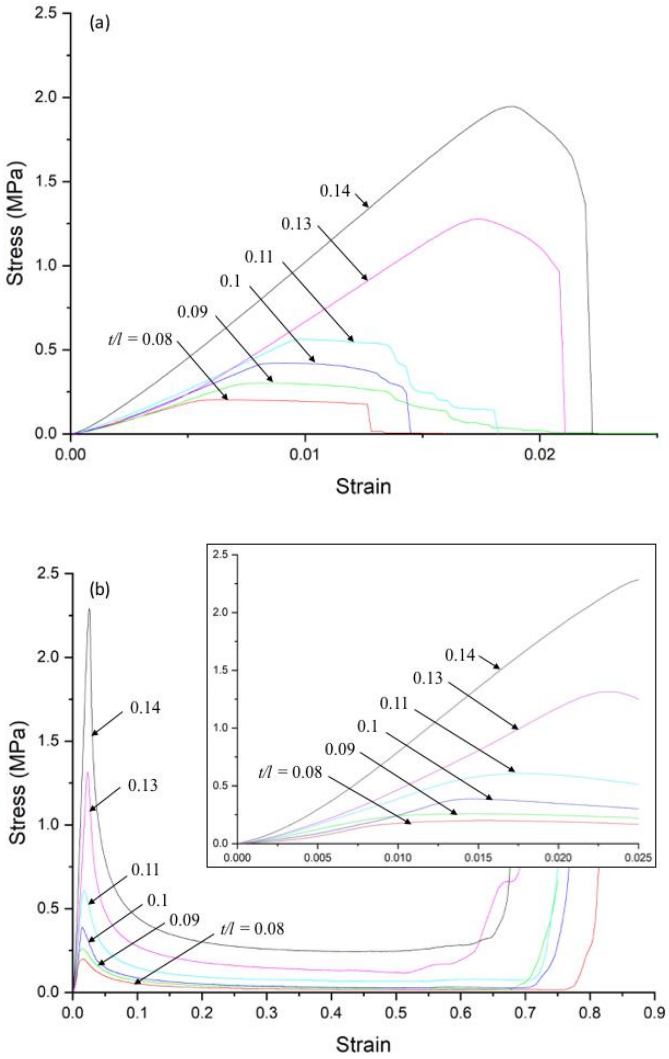

Figure 2-7: Out-of-plane compressive response of (a) cubic direct print and (b) cubic assembled lattice structures at different t/l values.

The stress-strain curves of the cubic assembled lattice structures are shown in Figure 2-7(b), with the initial peak stress ranging from 0.21 MPa for $t/l = 0.08$ to 2.33 MPa for $t/l = 0.14$. The maximum strain is considerably greater than those observed in Figure 2-7(a), indicating that the structure is capable of resisting load and absorbing energy with increasing strains in the post-buckled regime. Unlike in the cubic direct print structures, stress rises rapidly near the max strain, indicating a total crush and densification of the cellular structure. For example, densification starts

at $\epsilon \approx 0.8$ for $t/l = 0.08$ and gradually decreases to $\epsilon \approx 0.65$ as t/l increases to 0.14. The peak stress values for $t/l < 0.11$ are very similar in both direct print and assembled lattice structures. However, for $t/l > 0.11$, the peak stress in assembled structures surpasses that in the direct print structures.

To better examine the stress-strain response of the cubic direct print lattice structures, Figure 2-8(a) shows the photographs of the loaded structure at four distinct compressive strain values for the test article with $t/l = 0.11$. The lateral deformation of the struts is visible at $\epsilon = 0.009$. A closer look indicated that crack initiation began around $\epsilon = 0.014$ with rupture at $\epsilon = 0.019$ near the strut joints in multiple locations, highlighting the eventual cause of failure in these structures. It is also worth noting that failure was reached in a very short time after the quasi-static loading was initiated.

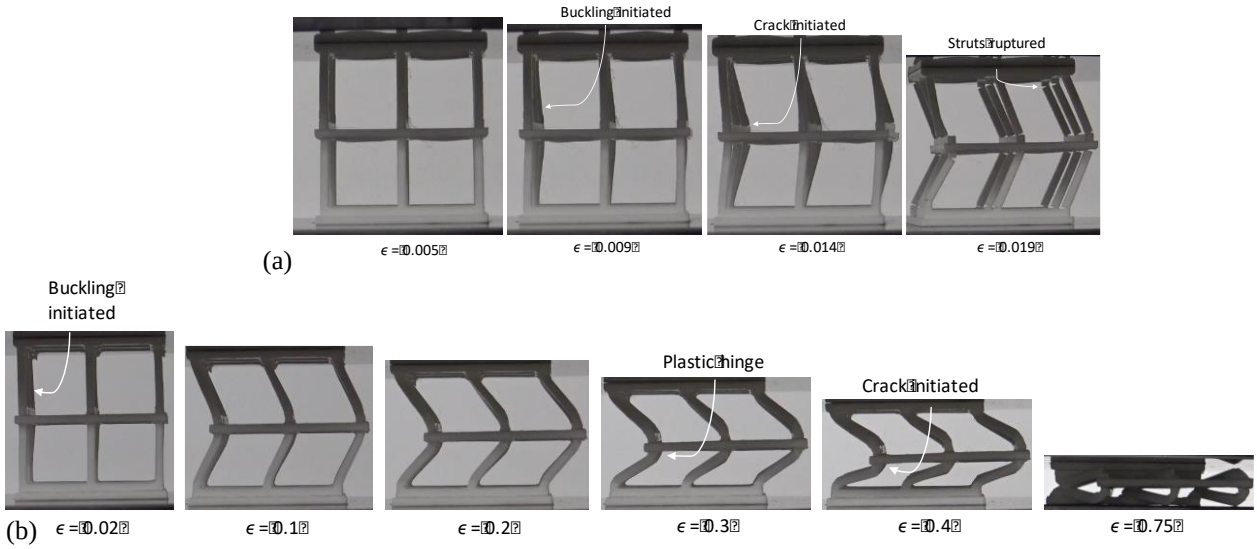

Figure 2-8: Compressive behavior of (a) cubic direct print and (b) cubic assembled lattice structures for $t/l = 0.11$.

The photos in Figure 2-8(b) highlight the progressive collapse response of one cubic assembled lattice sample with $t/l = 0.11$. Unlike the cubic direct print, crack initiation did not begin until $\epsilon \approx 0.4$ or later. A similar trend was observed in all the cubic assembled lattice structures regardless of t/l values. The plastic hinge formations observed at the nodes in Figure 2-8(b) demonstrate that the adhesive-bonded joints have no noticeable detrimental effect on the mechanical performance of the assembled lattice structure.

The differences observed in the cubic direct print and assembled lattice structures are mainly attributed to how each lattice is printed. In the cubic direct print lattice, the filaments are oriented in planes that are parallel to the cross-section of the struts generating contour plurality, whereas, in the cubic assembled lattice, the filaments are aligned along the axis of the struts, which eliminates contour plurality. When struts experience buckling-induced lateral bending, each strut cross-section experiences compression on one side and tension on the other. The formation of cracks and rupture in the struts, as seen in Figure 2-8(a), gives a clear indication of weak inter-layer adhesion aggravated by intrinsic porosity and the smaller contact area between filaments in direct print struts, which ultimately result in a tensile failure.

In the case of octet lattice structures, both direct print and assembled specimens demonstrate a similar compressive response at different t/l values as captured by the stress-strain curves in Figure 2-9 and the photos in Figure 2-10. The initial peak stress occurs at lower strain levels as density is reduced in both cases. For example, at $t/l = 0.08$, the initial peak stress appears at 3% strain in direct print and 4.5% strain in the assembled lattice. The pattern is consistent with that found in the recent work that simulates the peak stress for $t/l = 0.02$ to occur at 0.4% strain for octahedral truss unit cell [40]. The presence of the second peak around $\epsilon \approx 0.4$ in Figure 2-9, not seen in Figure 2-7, is indicative of the formation of additional plastic hinges and a progressive

collapse of the octet lattice structures, which is also not hampered in any discernible way by the use of bonded joints in the octet assembled lattice structures. A nearly total crush and densification is observed in Figure 2-9 at $\epsilon \approx 0.55$ for $t/l = 0.14$ increasing to $\epsilon \approx 0.8$ for $t/l = 0.08$. Moreover, there is no evidence of delamination or fracture failure in any of the octet lattice structures before reaching $\epsilon \approx 0.4$, regardless of the fabrication method. Contour plurality still exists in octet direct print lattice; however, the contact area between filaments has increased due to the inclined struts.

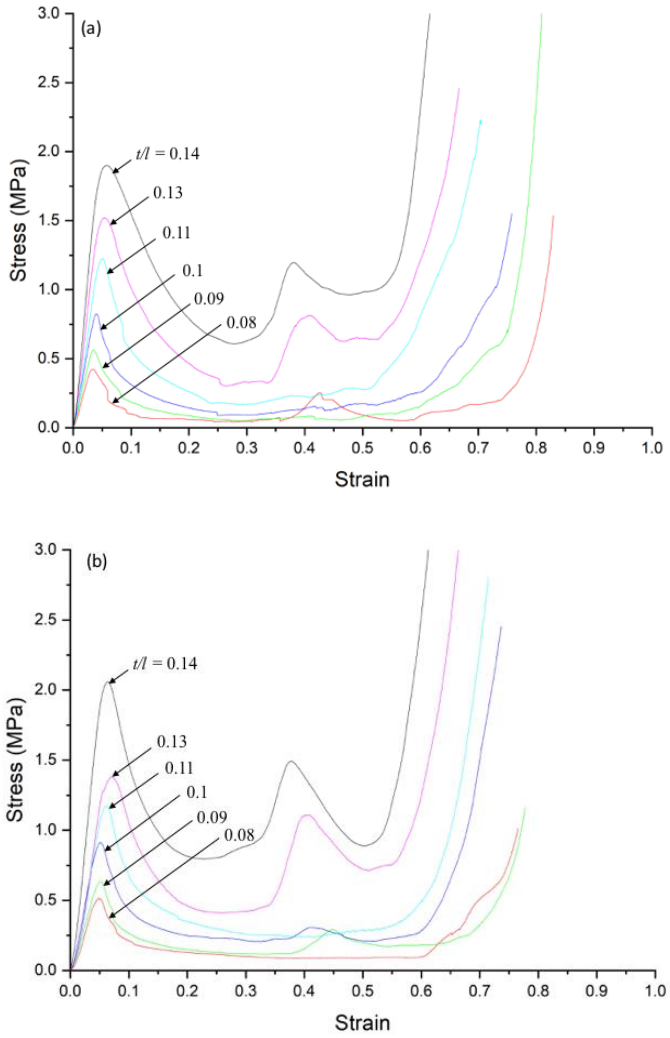

Figure 2-9: Out-of-plane compressive response of (a) octet direct print and (b) octet assembled lattice structures at different t/l values.

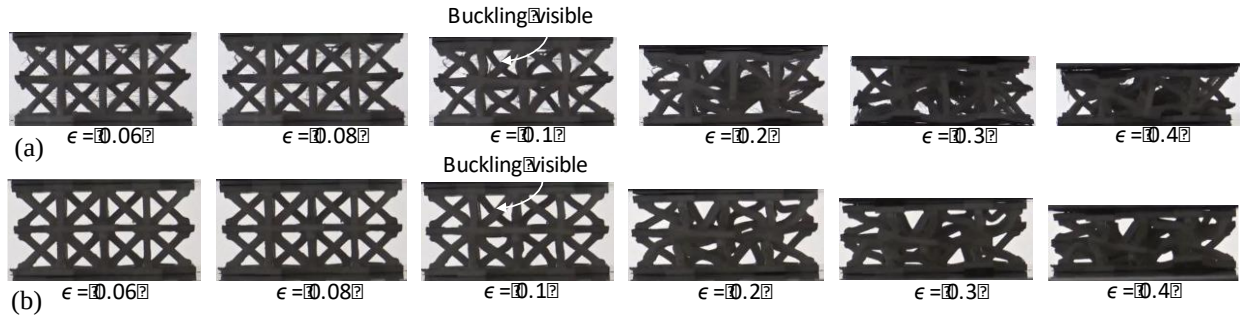

Figure 2-10: Compressive behavior of (a) octet direct print and (b) octet assembled lattice structures for $t/l = 0.11$.

As to the reasons for the differences observed previously in the cubic direct print and assembled lattice structures not being present in the octet direct print and assembled structures, we should look at the architecture of the struts in the cubic and octet structures. The struts in the cubic lattices are longer and have a larger cross-sectional area than those in the octet lattices, but the aspect ratios are roughly equal for similar t/l values. However, as shown in Figure 2-1, there are 12 struts between two adjacent horizontal layers in the cubic lattice, but there are twice as many (24) struts in the octet lattice structures. Also, whereas the struts are vertical in the cubic lattice, they are oriented at 45º in the octet lattice structures. Lastly, while in the cubic lattice structures, only two vertical struts are connected at each node from top and bottom, the strut connectivity in the octet lattice structure can be in one of two forms, as highlighted in Figure 2-1. Besides the architectural differences, there is a clear difference in how the applied compressive load is transferred to the lattice structure. A closer examination of the behavior in Figure 2-8 shows that the middle horizontal layer in the cubic lattice structures experiences no discernable out-of-plane displacement under loading. However, that is clearly not the case in the octet lattice structures (Figure 2-10), where the middle layer has to deform laterally in order to comply with the instability

and lateral deformation of the struts with increasing load values, which is quite visible at $\epsilon \approx 0.1$. What all of these differences point to is that the way the struts are loaded in the octet lattice structures makes their compressive response less sensitive to the filament orientation and inherent imperfections present in each printed layer, which is not the case for the cubic lattice structures.

The plots of specific energy absorption (SEA) for the cubic and octet lattice structures are shown and compared in Figure 2-11 as a function of t/l. The cubic assembled lattice structures outperform their direct print counterparts, with the difference being over ten times for all t/l values. In contrast, the difference in SEA for the assembled and direct print octet lattice structures is not as drastic but still significant, with the former being roughly 10 to 20% greater for all values of t/l. Comparing the range of SEA values by their more progressive and ductile response, the octet lattice structures can carry approximately three to four times more specific energy than their cubic counterparts. This characteristic would be useful in applications where energy absorption is an important design criterion.

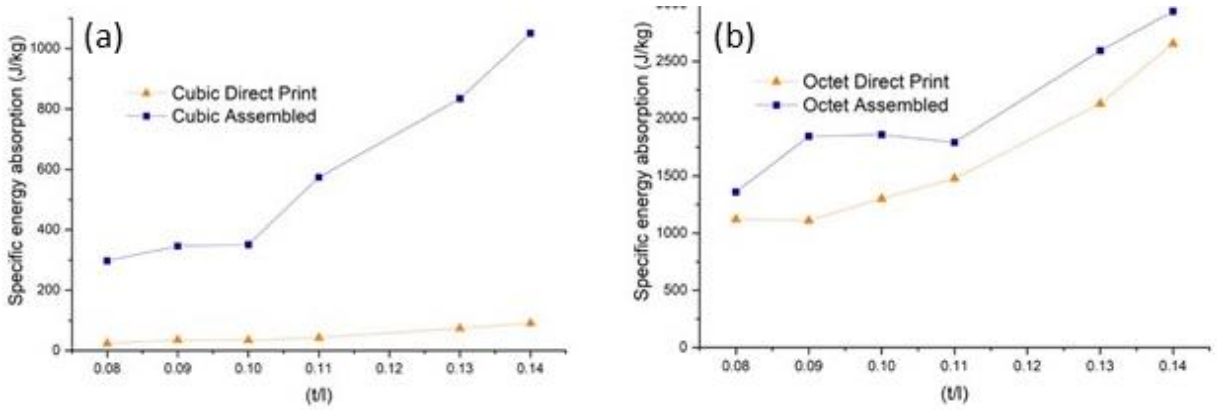

Figure 2-11: Specific energy absorption at different t/l values for (a) cubic and (b) octet lattice structures with different fabrication methods.

Table 2-2 compares the measured properties of the cubic and octet lattice structures with each other as well as in relation to the properties of the solid PLA as reported in the literature [41]. Since the compressive strength and elastic modulus of solid PLA are significantly greater than those of the lattice structures, the relative values shown in Table 2-2 for strength and modulus do not appear to vary considerably for different fabrication methods. However, the results discussed previously show that for the cubic lattice structures, the fabrication method can make a significant difference, whereas, for the octet lattice structures, it does not. Similar comparisons can also be made in terms of SEA and relative density.

Table 2-2: Measured properties of direct print and assembled lattice structures (σ_s= 60.6 MPa, E_s = 2.03 GPa [30]).

	Cubic Lattice		**Octet Lattice**	
	Direct print	**Assembled**	**Direct print**	**Assembled**
t/l	**Relative strength, $\frac{\sigma}{\sigma_s}$ (%)**			
0.08	0.35	0.35	0.71	0.88
0.09	0.51	0.45	0.96	1.07
0.10	0.73	0.68	1.39	1.54
0.11	0.96	1.04	2.06	1.98
0.13	2.16	2.21	2.56	2.33
0.14	3.28	3.85	3.20	3.47
	Relative elastic modulus, $\frac{E}{E_s}$(%)			
0.08	1.94	0.54	0.74	0.31
0.09	2.16	1.43	0.88	0.77
0.10	2.65	1.93	1.11	1.16
0.11	2.97	2.22	1.44	1.39
0.13	3.97	3.38	1.64	1.49
0.14	5.50	5.42	2.10	2.07
	Specific energy absorption (J/Kg)			
0.08	23.8	297	1121	1358
0.09	35.7	346	1110	1845
0.10	34.9	351	1300	1859
0.11	42.9	574	1478	1792
0.13	73.7	834	2131	2593
0.14	91.6	1050	2654	2936
	Relative density, $\frac{\rho}{\rho_s}$ (%)			
0.08	6.10	5.99	5.60	5.46
0.09	7.13	7.00	6.29	6.27
0.10	8.30	8.25	7.77	7.91
0.11	9.73	9.70	9.95	9.60
0.13	12.8	12.7	12.5	12.1
0.14	15.8	16.3	15.5	16.3

2.3.1 Prediction of strength and stiffness for octet and cubic lattice structures

The effective properties of octet lattice structures were developed by Deshpande et al. [42] using what is known as the DFA model, which was further modified by Dong et al. [39]. Depending upon the t/l, which also affects the relative density, $\bar{\rho}$, of the struts, the peak stress in the out-of-plane (z) direction, σ_{zz}, corresponding to elastic buckling and plastic yielding are estimated, respectively, as

$$\sigma_{zz} = \frac{k^2 \pi^2 E_s \sqrt{2}}{6} \left(\frac{t}{l}\right)^4 \tag{2.1}$$

$$\sigma_{zz} = 2\sqrt{2}\sigma_{ys} \left(\frac{t}{l}\right)^2 \tag{2.2}$$

where E_s and σ_{ys} represent the elastic modulus and yield strength of the base material, respectively. For PLA material, $E_s = 2.03$ GPa and $\sigma_{ys} = 60.6$ MPa [41]. Parameter k represents the column end fixity coefficient, which is bounded between 1 for pinned-pinned and 2 for clamped-clamped supports, with $1 < k < 2$ representing boundary conditions that provide partial rotational restraint that falls between the two extreme cases. According to the modified DFA model, the elastic modulus of octet lattice in the out-of-plane direction, E_{ZZ} is predicted as

$$E_{ZZ} = \frac{2\sqrt{2}E_s}{3} \left(\frac{t}{l}\right)^2 \tag{2.3}$$

Based on the data summarized in Table 2-2, the results obtained from Eqs. (2.1) and (2.2) are shown in Figure 2-12(a) while considering different values for k^2. The compressive strength and modulus values obtained experimentally in this study are also shown in the same figure. The analytical equation for elastic buckling appears to capture the compressive strength of the octet lattice structures by using $k^2 = 2$ for up to $t/l = 0.11$ and $k^2 = 1$ beyond that. Of course, as

shown in Figure 2-9, the drop in stress following the initial peak appears to be caused by a combination of buckling and plastic deformation, and the overall response of the structure cannot be characterized by elastic buckling. The modulus predictions from Eq. (2.3) appear to generally fall below the experimental results, as shown in Figure 2-12(b) for most t/l values, indicating that the octet lattice structure is stiffer than the analytical prediction.

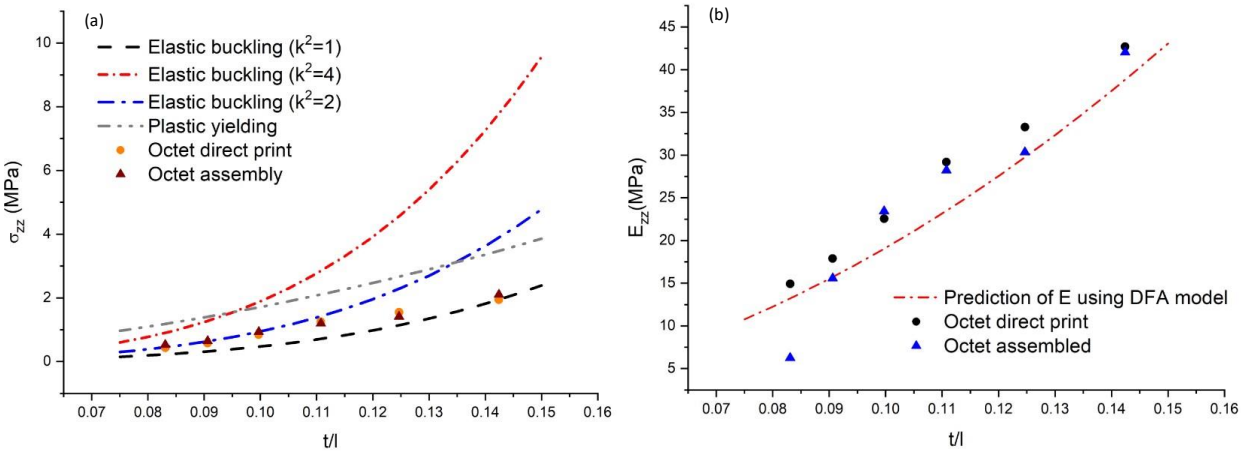

Figure 2-12: Out-of-plane compressive (a) strength and (b) elastic modulus for octet lattice structures at different t/l values.

The equations for compressive responses (i.e., stress and modulus) of the cubic lattice structure are derived in a similar manner as those presented earlier for the octet lattice structures. For the $2 \times 2 \times 2$ cubic lattice structure, the peak stress, σ_{zz} corresponding to elastic buckling and plastic yielding are estimated, respectively, as

$$\sigma_{zz} = \frac{3}{16} k^2 \pi^2 E_s \left(\frac{t}{l}\right)^4 \tag{2.4}$$

$$\sigma_{zz} = \frac{9}{4} \sigma_{ys} \left(\frac{t}{l}\right)^2 \tag{2.5}$$

The elastic modulus, E_{zz} for a $2 \times 2 \times 2$ cubic lattice structure can be predicted as:

$$E_{zz} = \frac{9}{4} E_s \left(\frac{t}{l}\right)^2 \tag{2.6}$$

Equations (2.4) through (2.6) are plotted in Figure 2-13 as a function of t/l for a 2x2x2 cubic lattice structure under out-of-plane compression. The experimentally measured values of compressive failure stress and modulus are also shown for comparison. As shown in Figure 2-13(a), at lower t/l values, the failure mode appears to be captured by the elastic buckling equation with $k^2 = 1$. When t/l increases, the failure mode comes closer to elastic buckling predictions with the strut joints providing partial rotational restraint with $k^2 = 1.5$ or in between the pinned-pinned and clamped-clamped boundary conditions. However, as shown by the photos in Figure 2-9, there is a distinct difference in the compressive response of cubic direct print and assembled lattice structures, with the latter showing evidence of both buckling and plastic deformation. This shows a different behavior than the stretch-dominated octet lattice structure. The aspect ratio of vertical struts decreases by increasing t/l which helps the strut absorb more energy before failure. Thus, in the 3D printed lattice structure, increasing t/l improves the joints of cubic structures compared to octet structures.

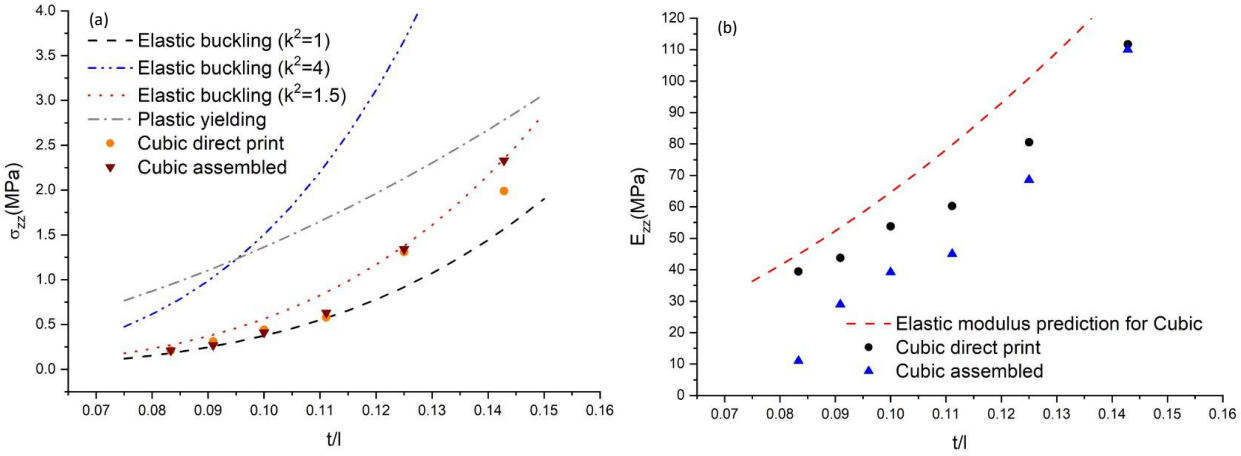

Figure 2-13: Out-of-plane compressive (a) strength and (b) elastic modulus for cubic lattice structures at different t/l values.

The elastic modulus data is plotted for both direct print and assembled cubic structures in Figure 2-13(b). It can be observed that the analytical equation over-predicts the elastic modulus for both direct print and assembled cubic structures. The primary reason for the difference is attributed to the fact that the struts are assumed to have a fully solid cross-section in Eq. (2.6), whereas they tend to have some level of porosity due to inter-bead voids that are present along the entire length of each strut. If porosity within the struts can be measured and included, the E_s value in Eq. (2.6) would be reduced depending on the average void volume fraction among the struts, and that would tend to shift the curve downward and closer to the experimentally measured values. The fact that the measured modulus for the cubic direct print lattice structures is higher than the corresponding assembled lattice can be attributed to both higher inter-bead voids as well as the presence of adhesive bonds, which tend to be more flexible than PLA in the assembled lattice.

To evaluate the performance of direct print and assembled lattice structures, their performance is analyzed using the Gibson-Ashby model of cellular solids [43]. The performance of porous structures decreases with the topology and their relative density. This loss of performance is often

expressed with a quadratic or higher-order scaling relationship [1]. The comprehensive study by Gibson-Ashby represents the relationship between specific performance to the specific density, which is also known as a power law. Based on the failure mode analysis, plastic hinges during failure is observed. For such a failure mode, the performance loss has been expressed with the following equation.

$$\frac{\sigma_{\mathrm{latt}}}{\sigma_{\mathrm{ys}}} = \mathrm{C}\left(\frac{\rho_{\mathrm{latt}}}{\rho_{\mathrm{s}}}\right)^{\mathrm{n}} \tag{2.7}$$

Here, ρ_s is the solid material density, ρ_{latt} is the volumetric density of the lattice structure which can be varied by changing the geometric parameters during structural design. σ_{latt} and σ_{ys} are the peak strength of the lattice and yield strength of the material, respectively. The exponential constant n indicates the loss of mechanical elastic property due to a reduction in relative density, which is determined empirically. Additionally, the mechanical performance loss has been attributed to constituent material properties, cell type (e.g., FCC, BCC, Cuboid) [44], and arrangement of struts (i.e., number of struts joined at each node) [45]. Such geometric constants of proportionality are included in coefficient C. The expected value for bending-dominated (cubic) structure is reported as $n = 1.5$, and for stretch-dominated (octet) structure is reported as $n = 1$ for plastic hinge failure [43], [46].

To determine the empirical constants n and C, Eq. (2.7) was plotted on a logarithmic scale (Figure 2-14), and the results are provided in Table 2-3. A distinct difference between cubic and octet lattices can be observed in the n and C values due to their geometric load-bearing efficiency through the strut. The arrangement of the strut is often expressed via bending-dominated vs. stretch-dominated structure by using Maxwell's number defined as $M = b - 3j + 6$ [47]. Here, b is the number of struts, and j is the number of joints of the lattice unit cell. For $M < 0$, the structure

is expected to be bending dominated or under-stiff, and otherwise, the structure may be stretch dominated or over-stiff. For a bending-dominated (fixed joint) cell, the value of n is often reported $= 2\sim3$, whereas $n = 1\sim2$ has been reported for a stretch-dominated lattice [35], [48]. The current experiment consistently matches these empirical constant value ranges for both direct print and assembled lattice structures, demonstrating the fabrication fidelity.

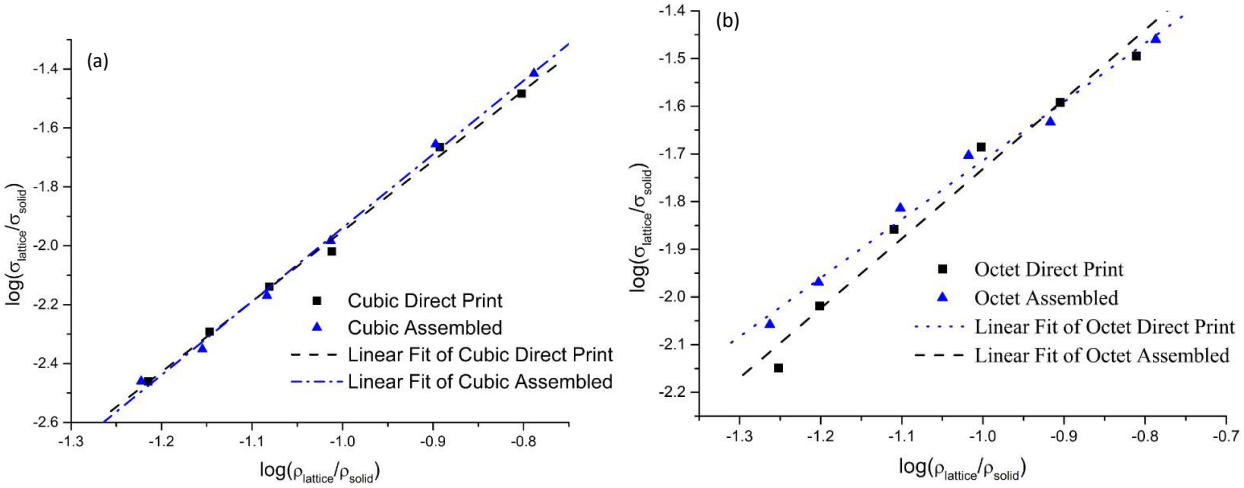

Figure 2-14: Log-log plot of peak strength ratio vs. density ratio for (a) cubic and (b) octet lattice structures.

The empirical n and C do not account for material and manufacturing imperfections in the equation [9, 22]. It should be noted that the suggested values for the empirical constants n and C are determined assuming homogenized properties applicable to large lattice structures where the boundary effects may be ignored. However, their experimental values shown in Table 2-3 are used to simply demonstrate the relative differences between the two manufacturing methods based on a common standard. Although the direct print and assembled cubic structures have the same nodal connectivity and geometric layout, they did not perform the same due to different intrinsic defects in the two manufacturing methods. The defects in the direct print lattice structures are due to

interlayer adhesion and surface roughness of the struts, including contour plurality. The proposed assembled structures fabrication technique is designed to minimize those issues and thus demonstrate better mechanical behavior (peak stress, energy absorption). The impact of filament continuity can be observed better in the octet assembled lattice structure, which has $n = 1.23$, where the direct print counterpart has $n = 1.46$ for the loss of strength, as shown in Figure 2-14(b) and Table 2-3.

Table 2-3: Value of the constants *n* and *C* for peak strength in Eq. (2.7).

	Cubic Lattice		**Octet Lattice**	
Constant	**Direct print**	**Assembled**	**Direct print**	**Assembled**
n	2.38	2.49	1.46	1.23
C	2.73	3.62	0.53	0.32

2.4 Conclusions

The effects of filament deposition following Eulerian path on the mechanical performance of direct print and assembled lattice structures were investigated. Both bending-dominated cubic and stretch-dominated octet lattice structures were printed using the assembled technique and compared with traditional direct print structures. Due to the continuity of the filament deposition, both assembled lattices experienced buckling and progressive failure through the formation of plastic hinges, making the assembled lattice structures suitable for energy-absorbing applications. For the direct print lattice structures, the architecture made a difference, with the cubic lattice failing due to fracture shortly after buckling while the octet lattice structure continued to exhibit progressive failure.

The proposed assembly technique makes low relative density lattice structures possible (<6%), which are often not viable in direct printing with the parameters used in this study. Similarly, the proposed technique also elevates the fabrication limitations of 3D printed lattice cell size and can print larger than 24 mm cells. This also allows the printing of smaller cell sizes as no support structure is required for the intricate internal architecture. Since the strut sub-assemblies are printed in a horizontal orientation to ensure filament continuity, the strut angle can be varied and printed without support. This will allow the proposed assembly technique to print gradient or non-periodic lattice structures, which may not be feasible through direct printing. Currently, the assembly time is insignificant due to a relatively small number of unit cells. However, as the number of cells is increased or the lattice itself becomes irregular, perhaps when conforming to a given shape or when different unit cells are used in different areas, then the assembly time must be included in comparing the manufacturing efficiency of assembled to direct print lattice structures.

CHAPTER 3 : METAL LATTICE MANUFACTURING USING EULERIAN WIRE STRUCTURES

3.1 Introduction

Due to the recent advancements in metal 3D printing technology, manufacturing of a wide-range of lightweight metal lattice structures using these processes became possible [49]. This technology uses low-dimensional raw materials, like molten filament or powder, which are incrementally consolidated. 3D printing is considered a rapid manufacturing process to construct a virtually constructed design of lattice structures [49]. Among the seven categories of additive manufacturing classified by ASTM, material extrusion method [50] and powder bed fusion [51], [52] can be used to fabricate very complex structures, including metallic lattice structures. For manufacturing metal lattices, the material extrusion method, also known as the direct ink method, can be used with raw materials like aqueous or polymer-based metallic ink [53]. However, manufacturing a thin section or a narrow lattice strut can be challenging as this method is prone to flaws like internal pores, cracks, rough surface finish, and warping due to shrinkage.

The quality of a metal lattice manufactured by powder bed fusion relies on the temperature source, the process parameters, and the post-processing measures taken. Selective laser melting (SLM), a type of powder bed fusion that uses laser to melt raw metal powder, can result in unstable microstructures [9], [51], disconnected struts, and warping [15] due to uncontrolled thermo-mechanical behavior of the process [54]. On the contrary, a highly controlled preheated vacuum environment in the electron beam melting (EBM) method makes the process significantly controllable. This technique can produce lattice struts with negligible thermal residual stress, which makes this process beneficial for manufacturing lattice structures [19]. Although metal

lattices from nano to macro scale are fabricable using metal 3D printing processes, manufacturing and geometric imperfection [55] with low surface quality [52], [56] and the huge initial cost of production makes them infeasible in general use.

Other techniques of manufacturing open-cell metal lattice other than 3D printing are robocasting [14], investment casting[18], coating in sacrificial mold [15], interlocked modular design [57], [58], and diffusion bonding of titanium alloys [17]. Robocasting uses a robotic deposition process to print with metallic ink. This process is heavily disrupted by nozzle agglomeration. A 3D printed sacrificial mold is used in the investment casting process. Liquid metal is cast into the mold, which faces some issues like early solidification and underfills. Coating with sacrificial mold also uses a polymer template like the previous method. This process uses the coating method of electroless nickel-plating for making hollow-tube metallic structures. The diffusion bonding of titanium alloy uses high-temperature forming to construct a sandwich structure with a pyramidal lattice core, which is generated by cutting a perforation pattern from a thin sheet of metal. This sheet is then bent and assembled into an interlocked periodic structure.

Metal lattices called “wire-woven metals” using a textile-based weaving process are becoming more prominent in manufacturing metal open cell structures [16], [59]. Straight wires are crimped or preformed into a specific pattern called “textilecore” [60]. These wires with symmetric geometries with wavy or helical patterns are ‘woven’ in separate groups from different directions to create Kagome or bulk diamond-type lattice structures. This set of woven wires is joined by various methods of soldering, adhesive bonding, brazing, or sintering. With this technique, large periodic lattices are manufacturable within a very short time, but heterogeneity and aperiodicity are not possible within the structure due to the weaving pattern. Because of the required extreme tolerance, unjointed nodes are usual within the lattice.

In this thesis, the manufacturing of complex lattice structures manufactured by bending 1D metal wires using a customized wire bending machine is investigated. This study is a continuation of the research done in these papers [10], [23], where the wire was bent in the 2D plane and manually bent to 3D to get cubic lattices. The primary objective is to find a method to construct 3D objects and more complex lattices with wire. The designs of the lattices described in this thesis have multiple separate unit layers, which are stacked and joined to get the final shape. The designs of the lattices are done in such a way that the intermediate unit layers are fabricable and stackable. In this method multilayer periodic or aperiodic lattice structure is also feasible. A bending machine is constructed with a specific design mindset, which allows it to construct the unit layers without any fabricability issues. The layers are then stacked and temporarily locked, which is called a loose lattice. Depending on the size and complex geometry, the nodes of the loose lattice can be inaccessible, and no traditional process can be applied to join them. The transient liquid phase (TLP) diffusion bonding process was investigated as it incorporates a dipping step in a liquid carrier system (LCS) which helps to access all the nodes. Because of the requirement of the vacuum furnace in the TLP diffusion bonding process, the design concepts are validated by making one layer structure and joining by regular soldering. The feasibility test of TLP diffusion bonding was also done for cubic-type lattice structures.

3.2 Manufacturing challenges of making 3D structures by wire bending method

Wire bending is predominantly used in making dental archwire in Orthodontics. Various research is done to improve the bending of a dental archwire. The improvement of the wire bender was done alongside. Other applications are in sculpture and jewelry. Due to the precision and customization needed in making archwires, several types of machines have been developed. A desktop wire bending machine called LAMBDA can manufacture a dental brace only using the x

and y axes [61]. It also contains a heating system to make the bend permanent. Due to its simplicity, this robot cannot make more complex 3D parts than a dental brace. To be able to make more complex structures, an approach with a six-degree of freedom robot with a gripping unit was employed [62]. This robot, including the gripper, has a heating mechanism like the previous one. A commercial version of a similar robot was distributed with the name of SureSmile [63]. Jin-jiang et al. [64] proposed a wire bending machine with a wire feeder, a fixed die or pin from the bottom, and a rotational die or pin from the top to make a 3D structure. This type of design is very efficient in bending at a small angle with versatility, but the space occupied by the fixed and rotational die system obstructs the 3D bending opportunity. A CNC design proposed by Hamid et al. [65] also has the option to rotate the bending mechanism, which is relatively big to have a small continuous 3D structure. A desktop wire-feed prototyping machine was proposed by Chang et al. [66], which can bend a wire and simultaneously join wires with a platform with 2 degrees of freedom. Other machines like automatic bending archwire machine (ABAM) [67] and cartesian robot for wire bending [68] all have the capability to bend 2D and, in some cases, a structure with a 3D shape but lack the capability to make a 3D structure directly from the machine. A theoretical study was done on finding the sequences of 3D wire bending by France et al., but bending tool space was not considered in this study. Figure 3-1 shows different types of bending machines previously used.

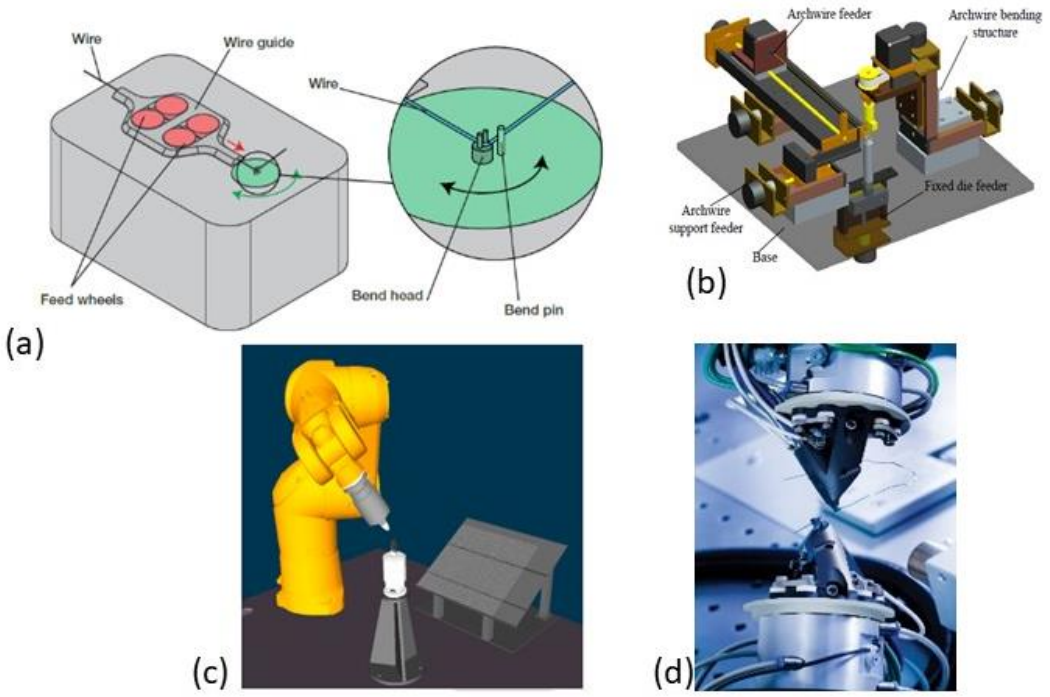

Figure 3-1: (a) DiWire by Pensalab[69], (b) Desktop bending machine [64], (c) Wire bender using ROS [62], (d) SureSmile Robot [63]

Bending a continuous straight wire to a 3D shape has its unique challenges. Previously Pensalab, with their commercial wire bender Diwire attempted to make a bending machine with a 3D shape manufacturability. They presented their first 3D bendable design but later discarded it because of the self-hitting of the wire, or wire hitting the device itself. This problem is further explored by Lira et al. [70] . They made a replica of Diwire's design and showed that to achieve certain wire sculpture shells, some specific fabricable Eulerian wire designs can be manufactured through the bending machine shown in Figure 3-2, which are then assembled to get the final shape. Lira et al. tried to confirm fabricability by taking small parts that are fabricable and combining them as they are separately fabricable. With this approach, they could optimize the wire path while bending, but no study has been done on whether the fabricable parts are stackable to have a final piece. Hence finding a proper solution is still in question.

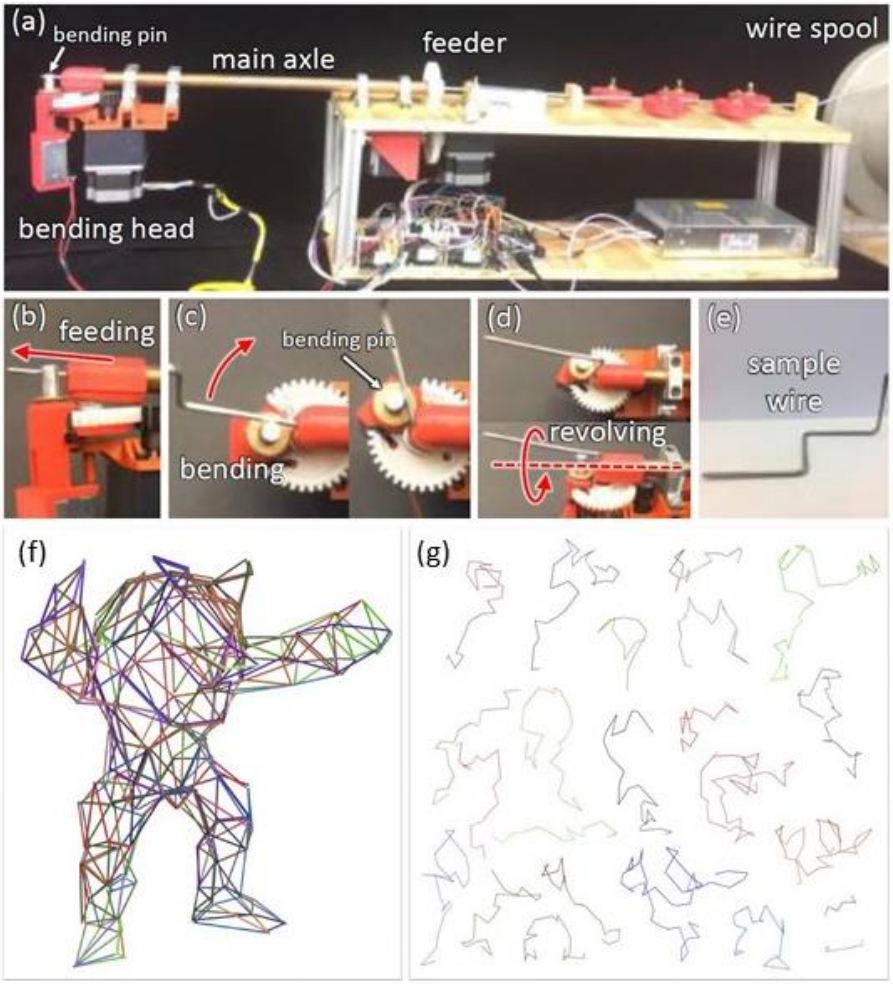

Figure 3-2 : Eulerian wire for sculptures, (a)-(e) Process demonstrated by Lyra et al. [70] for making a fabricable wire part. Bending a 3D structure from a bending machine. (f) and (g) shows the ARMADILLO model digitally manufactured by fabricable sub-parts.

To demonstrate the difficulty of a bending machine to make a 3D structure, a generalized bending machine can be imagined for studying the bending operations. The final bending machine is designed following the understanding of 3D bending machine's capability and limitations. The bending machine needs to have a wire holder and a feeder within the system shown in Figure 3-3. The machine itself will occupy a space which is unusable as the wire cannot go through the machine or itself. A bending mechanism is needed which can be attached to the machine from the

bottom or from the top. In this analogy we will consider it attached from the bottom to have maximum space. There are two ways to rotate the bent part in 3D we can achieve it by two ways: firstly, allowing the bending mechanism rotate; secondly, letting the wire itself rotate about its own axis. We will consider the later one. Some machines use a stopper die or pin to counteract the bending pin movement, but it also takes up space to obstruct the 3D part. We will assume the wire holder will act as a stopper pin to counteract the bending pin motion and help the bending process.

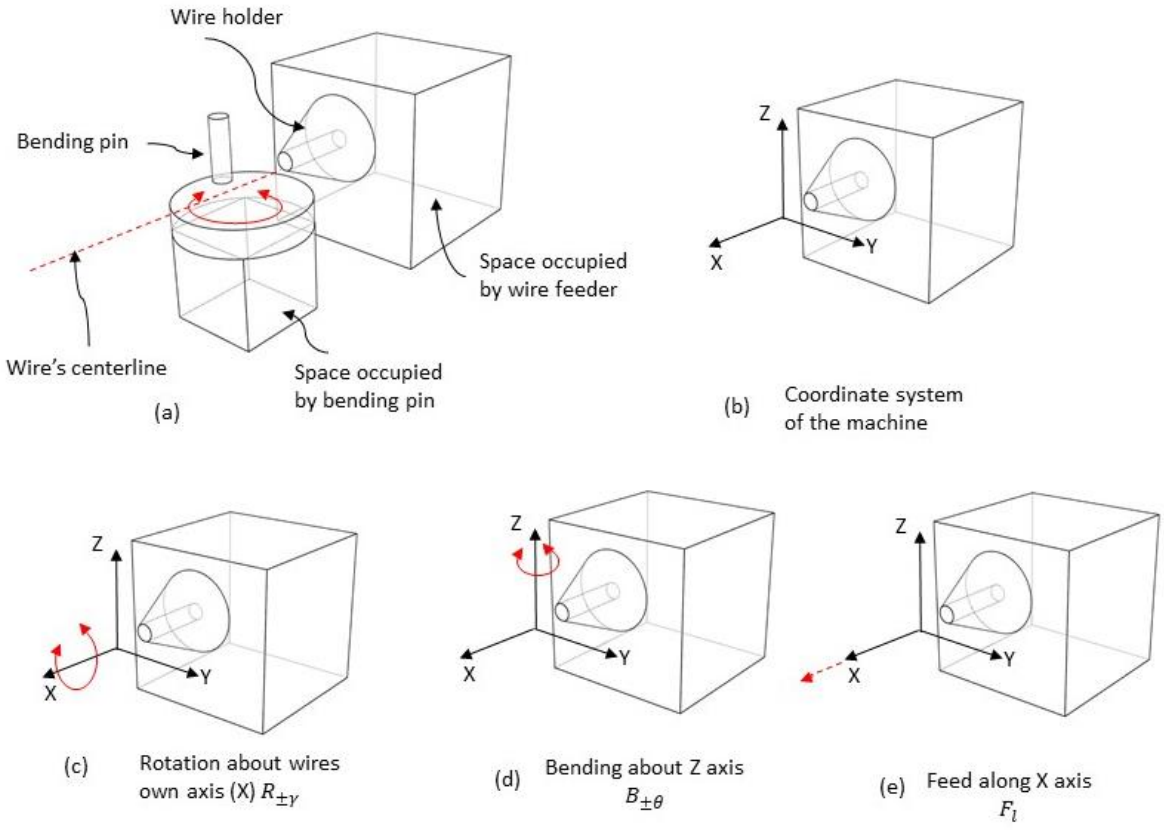

Figure 3-3: A generalized form of a wire bending machine with its coordinate system and nomenclature. (a) A wire bending machine consist of a wire feeder, wire holder and a bending pin with their occupied spaces, (b) coordinate system, (c) rotation about wire's own axis, (d) bending about Z-axis, (e) feed along X-axis.

Let us see with an example that how the self-hitting of the wire can halt the 3D structure fabricability using a wire bending process. Let us consider a cube (unit cell of a primitive cubic structure) that we want to manufacture using only a bending machine with a wire feeding mechanism, wire holding mechanism, and a wire bending mechanism. The input would be the straight wire, and the output would be the complete cube structure itself with the nodes presumably loosely touched with each other. The cube has 12 struts in its unit cell with 8 nodes (Figure 3-4(a)). All the nodes' topological orientations are the same, so we can start bending from any node. A continuous wire is fed through a bending mechanism (Figure 3-5), and each bend of the wire is obtained by rotating the bending tool clockwise or counter-clockwise, depending on the direction of the bend. The bending mechanism with the tool can rotate with respect to the wire, or the wire can rotate with respect to the bending tool, which is technically the same in this case. From Figure 3-5, we can see that it is possible to bend from node 1 to node 4, but the bend requires to go from node 4 to node 1, which is impossible as the wire will have to hit or go through itself to make this move. If we skip the move, for now, we can go to nodes 5, 6, 7, and 8, respectively, without hitting the wire or bending mechanism. But again, we cannot do anything else from here because of the 'wire hitting itself' situation. For a primitive cubic structure, 5 struts are missing out of 12 (Figure 3-4(b)).

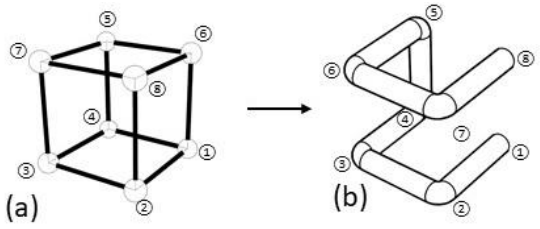

Figure 3-4: (a) Primitive cubic unit cell with nodes numbered, (b) fabricable structure from a bending machine.

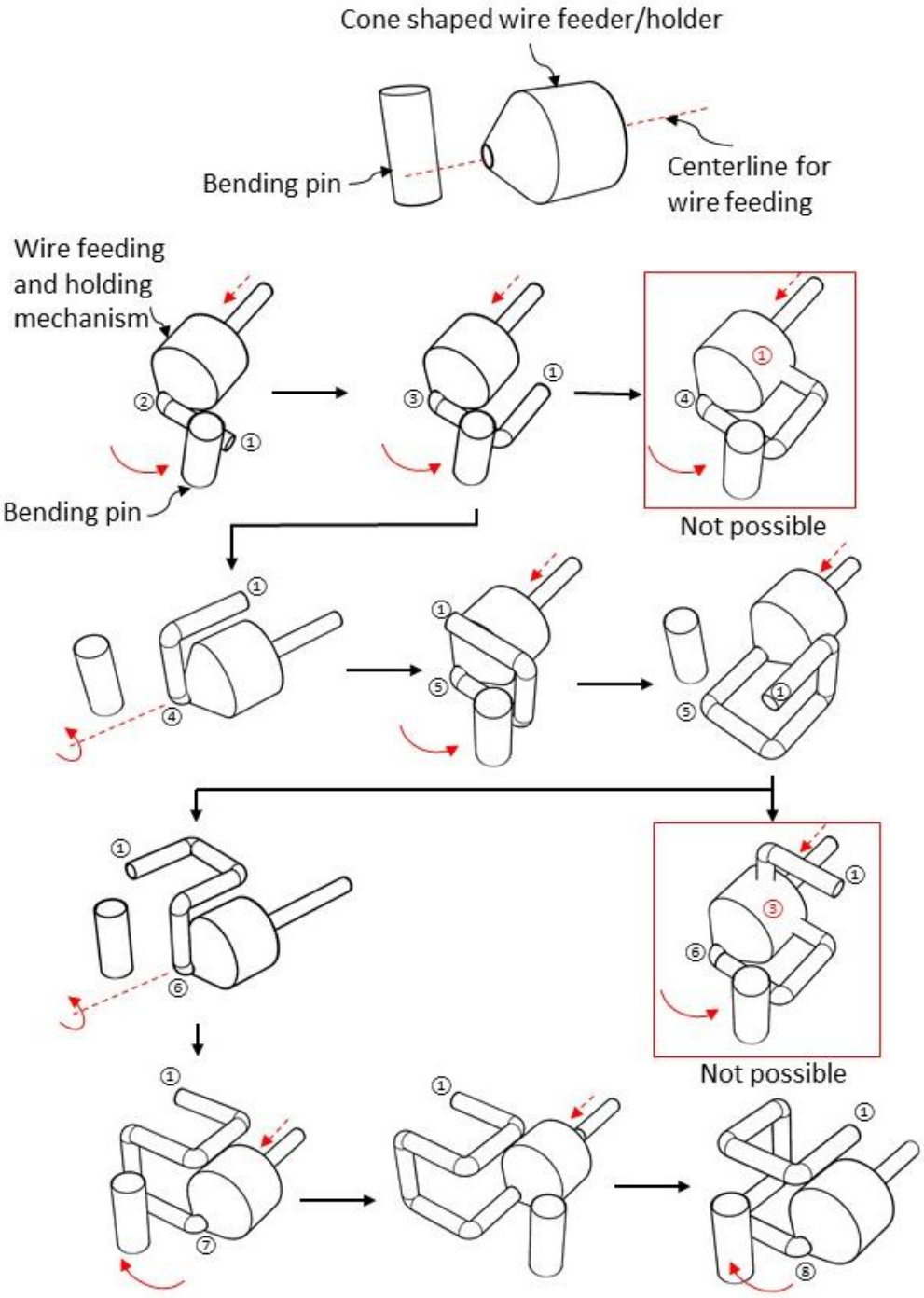

Figure 3-5: Bending operations required for obtaining a fabricable primitive cubic unit cell

The missing strut count can be further reduced if some manual bending and overlapping of struts is allowed. If we extend the layer shown in Figure 3-6, for the cubic, the extended part shown in

the left picture can be manually rotated and bent to decrease the missing struts. This process can further decrease the missing struts count to three but engages one overlapping strut, which is undesirable because it will increase the structure's weight.

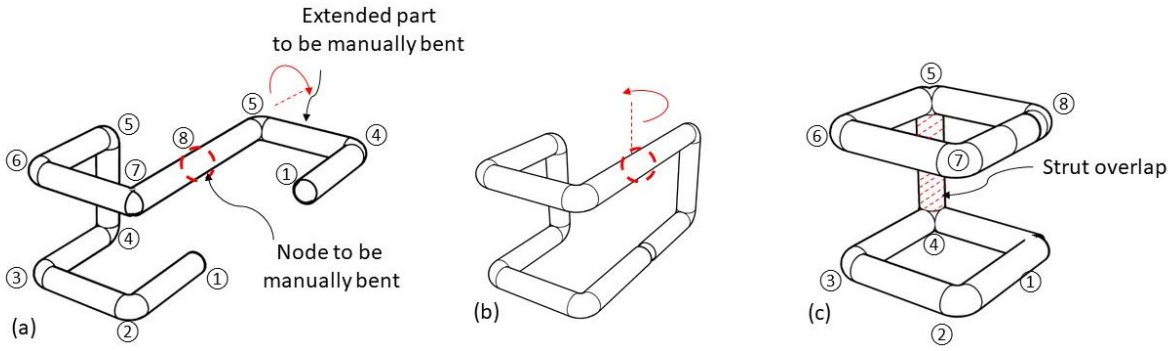

Figure 3-6: Allowing manual bending to cover more missing struts, (a) extending the fabricable cubic structure, (b) intermediate step, (c) structure after manual bending with overlapping.

Currently, there is no mathematical formulation for finding fabricable wire bent structures as bending is a global phenomenon [70]. The problem of finding a fabricable path without manual effort and missing struts can be relatable to an eighteenth-century problem called The Königsberg bridge problem (Figure 3-7(a)). In this problem, Mathematician Leonhard Euler tried to solve the problem of finding a route using the bridges around the islands in Königsberg, where someone has to use each bridge only once. Euler concluded that it is mathematically impossible to do that as each island has an odd number of bridge connections. He designated each island as one node and each bridge as one edge. Each node has a degree which is the number of edges from one node to other nodes. These degrees of nodes decide if a problem like this is solvable. The Eulerian path is defined from this analogy as discussed in Chapter 2. The existence of the Eulerian path is only possible in two cases. The first one is if each node has an even number of connectivity, meaning each island is connected with other islands with an even number of bridges. Secondly, if there are

only two nodes with an odd number of edges, the starting and ending node have to be one of those two nodes (Figure 2-3).

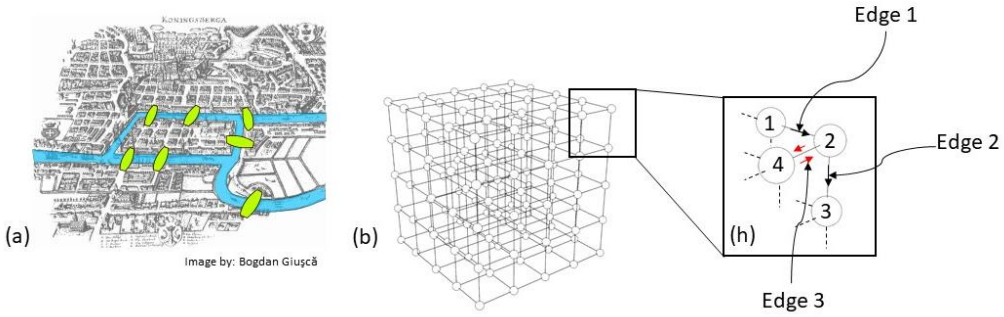

Figure 3-7: (a)The Königsberg problem, (b) corner of a big cubic lattice is enlarged in the inset, node 2 has three edges, which violates the criteria for being a Eulerian path.

If a similar analogy is applied to the problem of finding a fabricable path, it is possible to relate the edges or bridges in the Königsberg problem with struts in the lattice structures. The person who is crossing the bridges is analogous to the bending mechanism, which will take each path (strut) to go to the nodes and make a bend at that node. In a thought experiment it can be assumed that the bending mechanism going to each node of a straight wire and conducting the bends (Figure 3-9). It is the same as feeding the wire, but now the machine space can be evaluated between the designs.

Let us consider a corner of a big primitive cubic structure. The corner node is connected with other nodes with an odd number of struts which is three in this case. For a structure to be fabricable, the machine or the feeding mechanism can go through all the struts only once. If we do not allow any bending through the machine after the structure is built, the machine can go to each node only once. If there is an overlap or the node has an odd number of edges (in our case, struts), the path

for the machine is not Eulerian. So, the machine cannot do the bending without hitting the already constructed structure. From this analogy, it is comprehensible that it is not possible to have a structure directly bent from a machine that has any node with more than two strut connections (Figure 3-8). So to be fabricable, a bending pattern should follow an Eulerian path (using each strut only once). If we impose the rule that the machine can go to each node only once, the bending pattern must follow a path called the Hamiltonian path. The Hamiltonian path is the path which uses each node in a graph only once but does not necessarily use all the edges. So a design with a Hamiltonian path confirms the movement of the machine through all the nodes, but there can be missing struts in the structure as the path does not need to use all the edges.

It is to be noted that existence of an Eulerian path does not confirm fabricability. In other words, all fabricable structures follow the Eulerian path, but not all structures that follow the Eulerian path are fabricable. So, a fabricable output structure has to fulfill two necessary but not sufficient conditions:

(i) The path of the movement of the machine has to be an Eulerian path.

(ii) Each node of the Eulerian path can have a maximum of two edges.

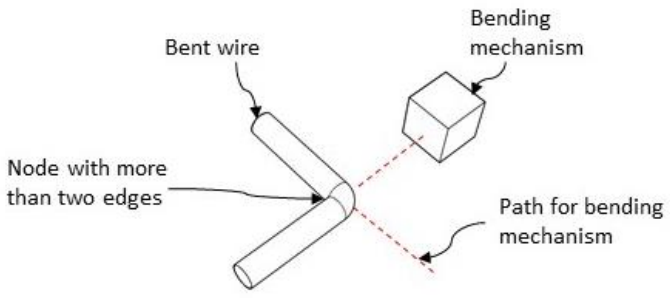

Figure 3-8: A node with more than two edges is impossible to fabricate via bending as the bending mechanism has to go through pre-bent wire.

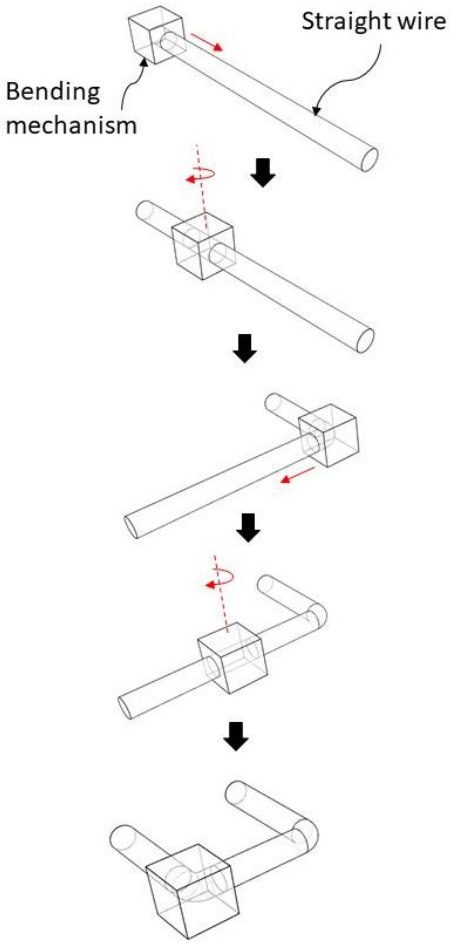

Figure 3-9: Assuming the bending mechanism is moving along the straight wire to do bends at certain nodes

3.2.1 Fabricability of a wire structure

To make a lattice structure using the wire bending method, unit layer structures that are fabricable are designed and stacked in the required orientations. This structures are noted as loose structures as the nodes are not connected. After that, a joining method is used to complete the manufacturing process of making lattices. It must be made sure that the unit layer structure is fabricable (the wire does not hit itself or the bending machine) and the structures are stackable according to the orientation required for the lattice.

By deeply observing the bending situations, some remarks were made to ensure the fabricability of a unit wire structure. The approach is to construct a 2D layer first, then shift the layer to another plane from the current bending plane to have a 3D layer-based structure.

First, we must confirm a design is fabricable in 2D. For the following reasons, the 2D designs can be in a situation of not fabricable:

- A 2D structure cannot be fabricable if the 2D design has a loop in it. In other words, if the bending machine visits the same node twice at any time following the instruction (Making a Hamiltonian Circuit, enough condition not to be fabricable). An example is shown in Figure 3-5, where an O loop is not possible due to the hitting of the wire itself.
- A 2D structure cannot be fabricable even if it does not have a loop in the design or the bending mechanism does not visit the same point twice. An example is shown in Figure 3-10. The spiral shape is bendable if the bending is started from point a. If started from point b, at step 4 of the bending process, it crosses the *XX'* line and hence hits the bending mechanism, making the 2D structure not fabricable. This phenomenon can describe as the bending machine is moving from an outward point to an inward point. While bending the bigger dimensions of outside is responsible for the bent structure to cross the *XX'* line. So, if a 2D wire structure crosses the wire feed line at any point during the bending operation, the 2D wire structure is not fabricable.

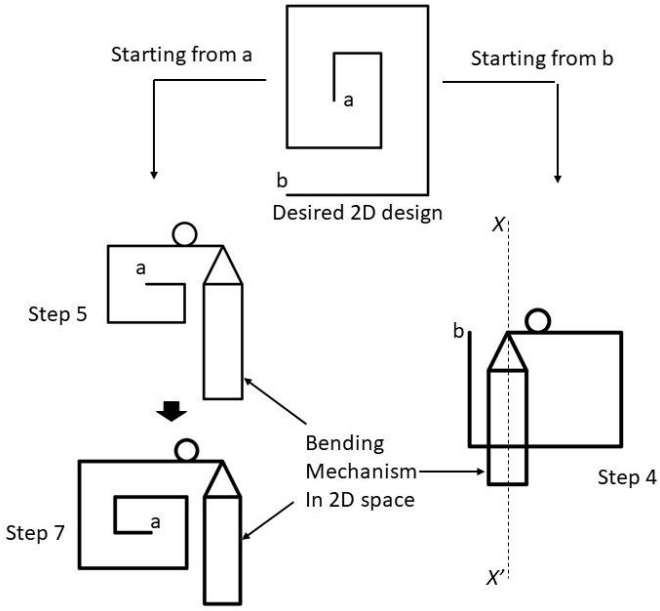

Figure 3-10: A desired spiral shaped design has a different situation if started from point a and point b. The part is fabricable from point a but not fabricable from point b, as it crosses the XX' line at step four of the construction.

After ensuring a design is fabricable in 2D space, we can shift the design to a parallel layer and start bending in a plane that is parallel to the previous plane (Figure 3-11) by following the necessary conditions. Let us introduce some notations to express certain actions (e.g., rotating and feeding maneuvers) in the machine:

- Feeding the wire is denoted by symbol *F* with the subscript denoting the amount of feeding in milimeter as *l.* So, feeding 10 mm with the wire feeder is transcribed as F_{10} (Figure 3-3(e)).
- Bending the wire is denoted by symbol *B* with the subscript of bending angle θ. So, bending a wire with a counter-clockwise rotation of 90º is transcribed as B_{90}. The rotation is evaluated from the top view (Figure 3-3(d)).

- Rotating the wire about its own axis as R with a rotation angle γ. So, rotating a wire with an counter-clockwise rotation about its own axis is transcribed as R_{90}. The rotation is evaluated from the front view (Figure 3-3(c)).

Now, to move a constructed plane (where the 2D structure is already done) to the parallel of the bending plane, we have to follow this maneuver:

$$S_{next\_layer} = R_{-90}B_{-90}F_{l_{interlayer}}B_{-90}R_{-90} \tag{3.1}$$

Figure 3-11 shows how this set of instructions moves the first layer up the bending machine and allows the bending tool to bend in a parallel layer without interruption. This maneuver will allow any already constructed layer or set of layers to the upper portion of the machine. Here, $l_{interlayer}$ is the distance between two fabricable parallel layer and must be bigger than half of the wire feeder or holder width dimension w_m. This is further elaborated in the design of the machine section.

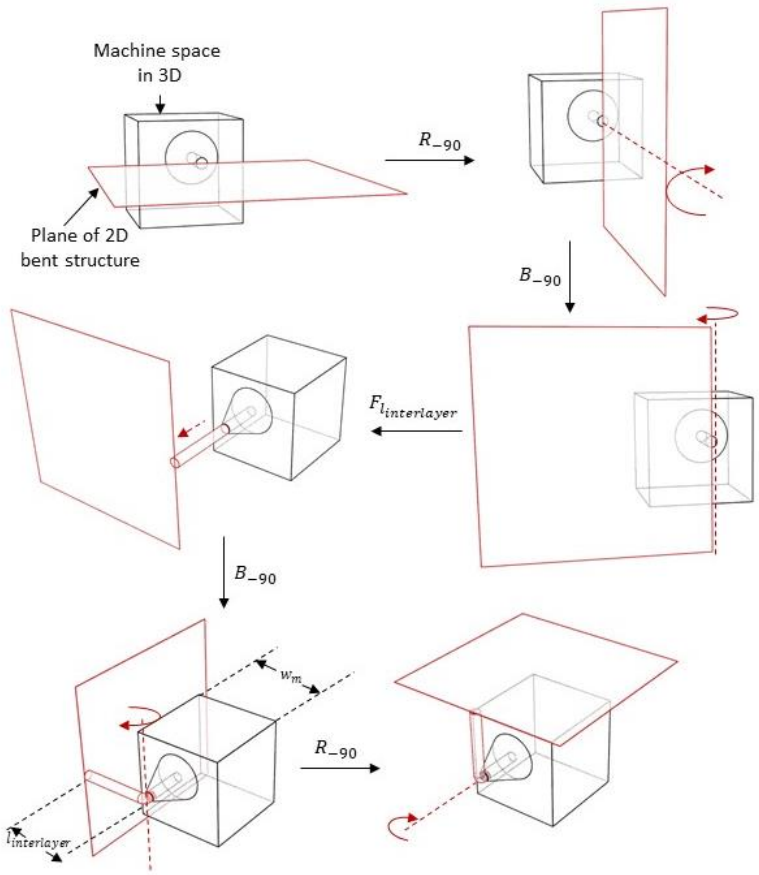

Figure 3-11: Bending sequence for shifting a 2D plane to a parallel plane, following the bending sequence of $R_{-90}B_{-90}Fl_{interlayer}B_{-90}R_{-90}$.

If a 2D layer is fabricable and the stated algorithm is applied, technically, the amount of the layers bent would be infinite (Figure 3-12) (practically, because of the weight of the structure, the part will sag over the bending tool and induce error). The length and width dimensions of the 2D layer cannot exceed in such a way it would hit the bending machine when the 2D layer is moved to the left (Figure 3-11, fifth step).

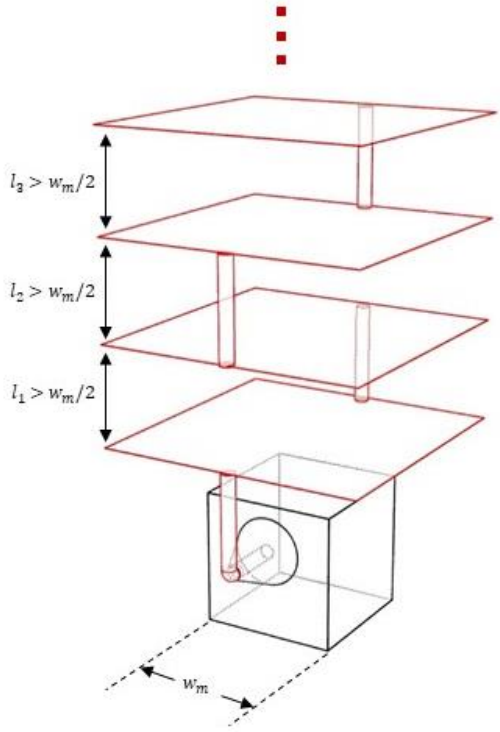

Figure 3-12: Shifting multiple planes parallel to each other, making a unit layer structure.

3.2.2 Unit fabricable structure

In this research, two types of fabricable unit layer structures are studied: (i) Triangular type and (ii) Square type. These two types of structures can be stacked to get almost every type of open strut type lattice structure. These two types can also be periodic or aperiodic. Periodic structure makes the topological properties practically the same all over the part. To have a topologically optimized part, process of manufacturing aperiodic lattices is necessary.

The triangle-type unit layer is constituted by triangle-shaped structures compiled in layers (Figure 3-13). It is achieved by bending the wire in an alternating way. θ can be from <180˚ to the smallest bend angle possible with the bending tool. The angles ($\theta_1, \theta_2, \theta_3, ...$) can be equal or not equal, depending on the periodicity or aperiodicity of the final structure. If the triangles need to be

aperiodic, but the nodes need to be in the same plane, the lengths of the struts (l_1, l_2, l_3, ...) need to be adjusted. The instruction set for one triangle unit cell is constructed as:

$$S_{triangle\_unit} = (F_{l_i} B_{-\theta} F_{l_{i+1}} B_{\theta}) \tag{3.2}$$

If there are k unit cells in the whole structure (considering one triangle shape is part of one unit cell), the instruction set would be as follows:

$$(S_{triangle\_layer})_k = \sum_{n=1}^{k} S_{triangle\_unit} = \sum_{n=1}^{k} (F_{l_{2n-1}} B_{-\theta} F_{l_{2n}} B_{\theta}) \tag{3.3}$$

This will make one layer with triangles. If there are multiple layers, the current layer needs to be shifted to the next layer by using Equation (3.1). If there are m layers in the unit structure, the instruction set should be as follows,

$$S_{unit\_layer} = \left(\sum_{n=1}^{m-1} (S_{triangle\_layer})_k + S_{next\_layer}\right) + (S_{triangle\_layer})_k \tag{3.4}$$

The square type of unit layer involves four bending angles and four struts as a unit repeatable instruction. The instruction for a square shape (all $\theta = 90^{\circ}$) should be as follows:

$$S_{square\_unit} = (F_{l_{v\_i}} B_{-\theta} F_{l_{h\_i}} B_{-\theta} F_{l_{v_{i+1}}} B_{\theta} F_{l_{h_{i+1}}} B_{\theta}) \tag{3.5}$$

Similar to the triangle type, the instruction set for a unit layer can be written as follows:

$$S_{unit\_layer} = \left(\sum_{n=1}^{m-1} (S_{square\_layer})_k + S_{next\_layer}\right) + (S_{square\_layer})_k \tag{3.6}$$

Instruction sets from Equations (3.4) and (3.6) can be applied using a Rhino visual basic code (.rvb) to make the G-code required for the bending machine which is stated in a later section.

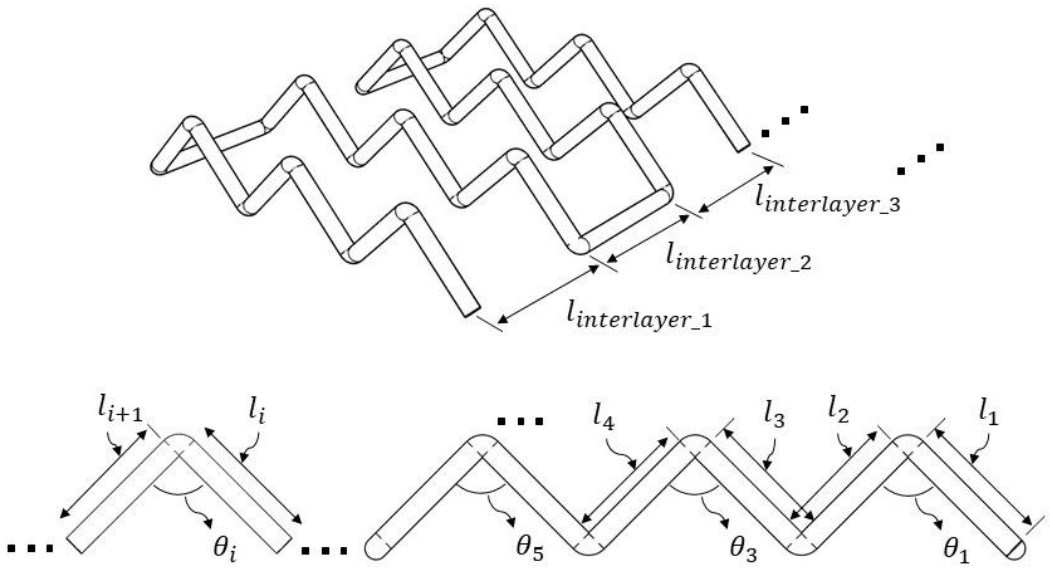

Figure 3-13: Unit layer structure with triangular repeating cells.

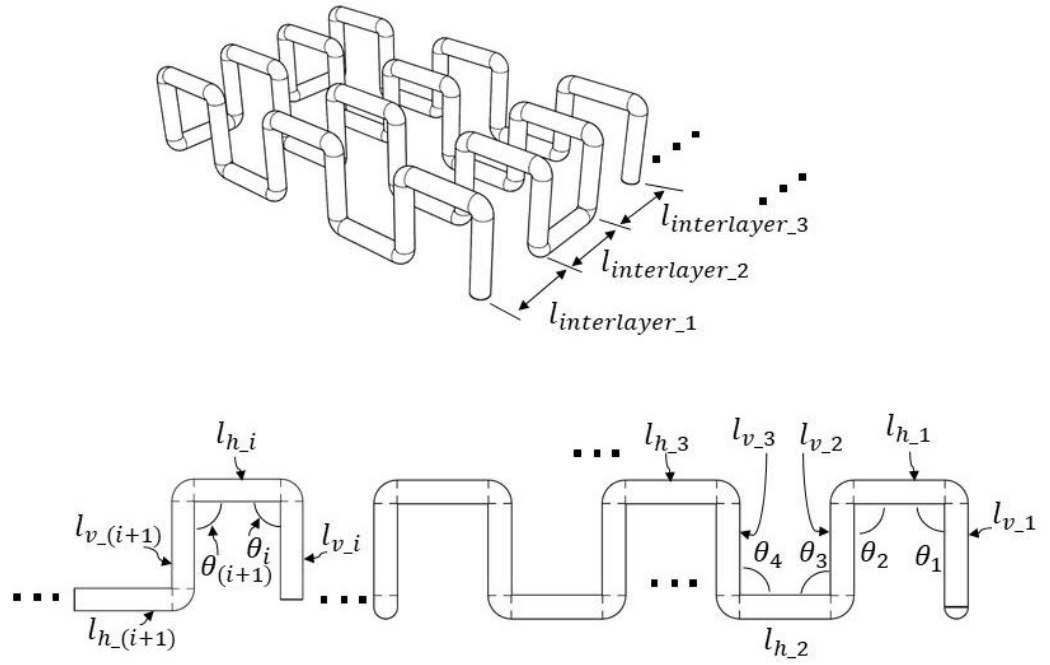

Figure 3-14: Unit layer structure with square repeating cells.

Equations (3.1)-(3.6) describe the bending operation for in-phase structures. The unit layer structures can be out of phase and still fabricable as it does not contradict any of the rules stated

before. By out of phase, it is meant that if one layer ends at the bottom, the next layer will start from the top and vice versa. Figure 3-15 shows out-of-phase triangular and out-of-phase square structures. Out-of-phase triangular structures can be beneficial as they are the core structure required for the BCC (body-centered cubic) or structures generated by stacking more layers over BCC. The bending operations set can be constructed for out-of-phase structures by shifting by one instruction in the equation after each layer and changing the angles in the next layer instruction in Equations (3.4) and (3.6).

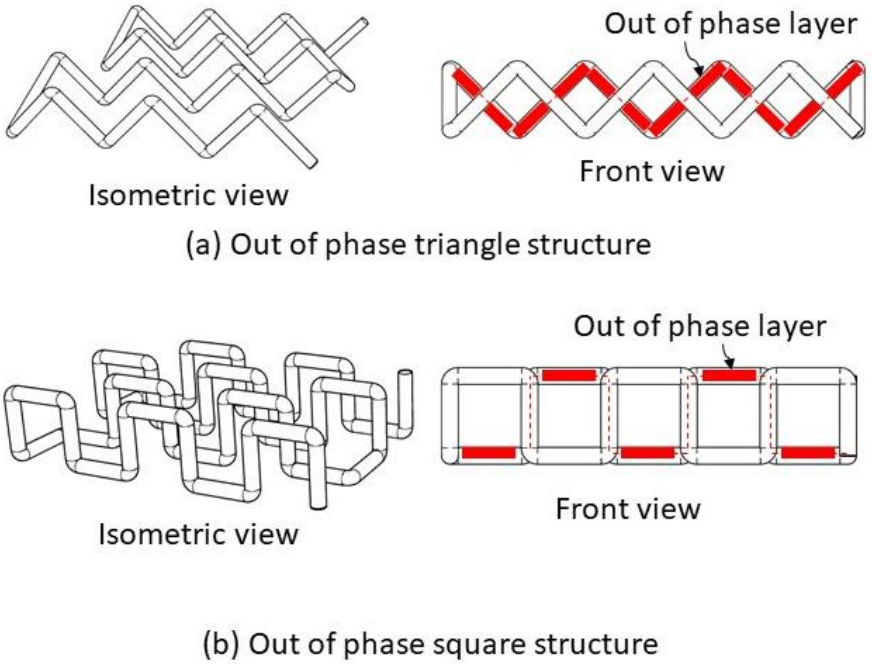

Figure 3-15: Out of phase unit layer structures (a) triangular, (b) square.

3.2.3 The stackable unit layer structure

Fabricable structures are not guaranteed to be stackable with each other. It is observed that two types of situations can occur in terms of ability to stack. In this thesis, they are referred to as first-degree and second-degree stacking. The first-degree of stacking occurs when two unit layer

structures are put one over another. The necessary condition to be stackable in this way is that all nodes need to be on the same plane for both structures. If the nodes do not align with each other, a node gap can occur, which will result in weak mechanical properties in lattice structures. Figure 3-16(a) shows an example of a first-degree stacking.

Second-degree stacking occurs when a unit layer structure needs to be insertable into another structure or set of structures. Basically, the group of structures will have a hole where the unit layer structure needs to be inserted. By observation, two types of effects were observed: hole topology effect and stacking chronology. The hole topology effect can be observed when a single unit layer needs to be inserted, where the insert structure cannot be bigger than the hole. Also, if the hole converges, the insert has to converge. If the hole diverges, the insert can only have a dimension less than the beginning dimension of the hole (Figure 3-12 (b)(i)). The second type of stacking issue can be observed if two or more unit layers need to be inserted into a base structure. The orientation and chronology can affect how we can stack unit layers one after another. If multiple inserts are to be stacked from different orientations, their stackability will depend on their topology. The left Figure 3-16 (b)(ii) shows that for some orientations; it does not matter what the stacking chronology is. But in the right figure stacking layer 1 first will block the pathway for stacking layer 2. But the opposite does not do the same. Stacking layer 2 does not block the hole for layer 1. So for stacking, some visual and 3D observation needs to be done beforehand.

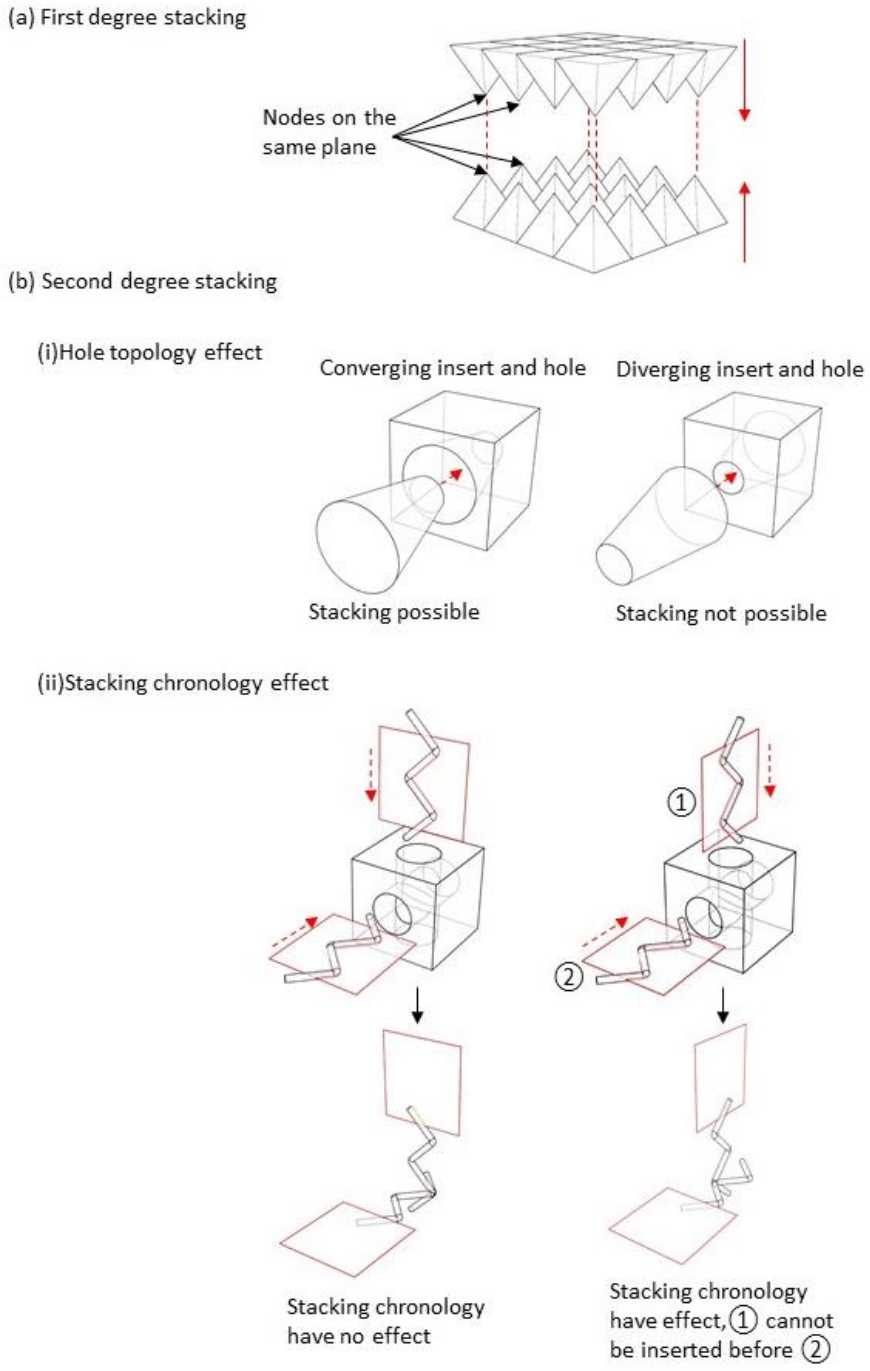

Figure 3-16: Analysis of stacking of different structures, (a) first-degree stacking, (b) second-degree stacking, (i) hole topology effect, and (ii) stacking chronology effect.

3.2.4 Node wrapping

Node wrapping phenomena needs to be considered while designing two stackable unit layers. Because of the diameter of the wire, two stacked layers' nodes cannot go through each other, and each node occupies some volume. Because of this, one layer's nodes need to wrap over another layer's nodes, and this defect cannot be solved in any way. This defect can be minimized by readjusting strut lengths and bending angles to have a perfect fit with each other, and together they will act as one node before stacking other structures.

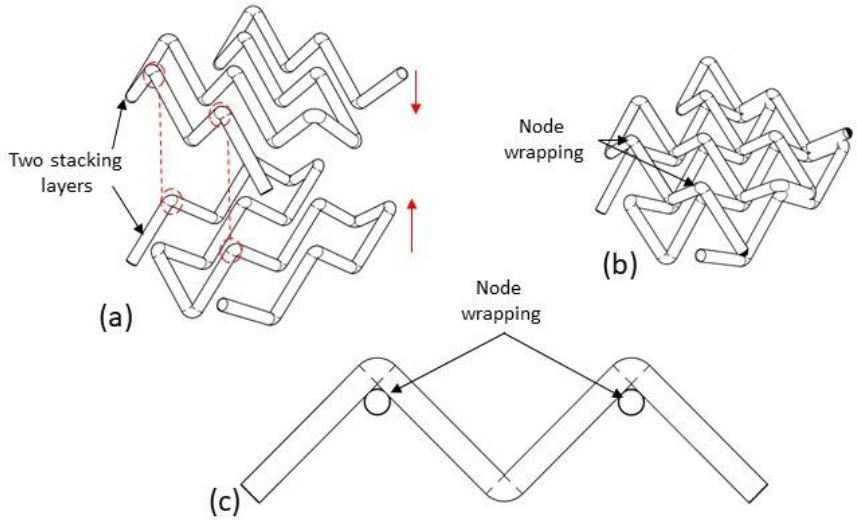

Figure 3-17: Node wrapping for two out-of-phase triangular structures (a) unit layer structures before stacking, (b) after stacking with node wrapping, (c) front view for node wrapping.

3.3 Manufacturing process of Lattice using Metal wire

3.3.1 Design of the bending machine

The bending machine is designed to have four degrees of freedom which are represented by the X, Y, Z, and W axes (Figure 3-18(a)). The X-axis contains the wire feed mechanism, which has a 450mm linear rail module and holds the carriage of the Y-axis rotation motor. The Y-axis is a rotary axis that is used to rotate the wire about its own centerline . The Y-axis motor is a hollow shaft motor with a hollow chuck in its head, which is to facilitate continuous bending of a straight wire. The total feed of the G-code will always be within the limit of the X-axis linear rail module, which is 450 mm. If a long G-code is needed to be applied, it is broken into sections. The carriage is stopped at the end of the X-axis, the chuck is loosened, the carriage is moved back while the wire with the bent structure is kept in its place, and again the next part of the G-code is started.

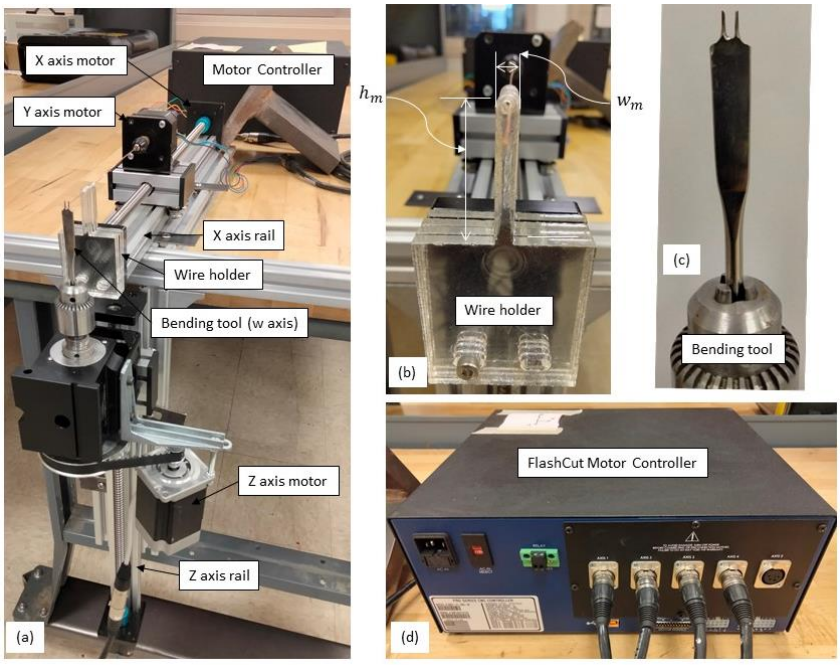

Figure 3-18: Parts of the bending machine, (a) Wire bending machine, (b) wire holder, (c) bending tool (d) FlashCut motor controller.

The Z-axis is used for engaging and disengaging the bending tool to the straight wire. The bending tool is a fork-like instrument whose centerline goes through the wire to execute the bending both clockwise and counter-clockwise Figure 3-18(c).

The whole system is driven by a controller system, “FlashCut” Figure 3-18(d). The G-code generated from the fabricability checking software is described in the next section. The G-code can be directly executed through the FlashCut CNC software to the FlashCut motor controller system. The CNC software needs to be calibrated with the motors before use.

The things that help the bending machine to make a practically infinite number of intermediate stackable layers are the wire holder and the bending tool system. The holder's dimension w_m and h_m, defines the lowest limit for interlayer distance and highest limit for the 2D plane’s width, respectively (Figure 3-18(b)). When one intermediate layer is constructed, to move to the next intermediate layer, the previous intermediate layer needs to rotate along the wire holder and the side of it, according to Figures 3-11 and 3-12. Therefore, the minimum intermediate layer distance must be bigger than $w_m/2$.

3.3.2 Checking the fabricability of a structure for a given instruction set

A custom visual basic based code is written to construct the G-Code and check the bending sequence to avoid any collision with the tool or the bending machine. The code’s input is the instruction set required for the unit layer structure. The code follows the instructions and visual interpretation of the bending and rotation performed by the instructions. While the code runs the visual interpretation, it simultaneously fills up the initially empty G-Code. If it is found that no self-hitting of the wire is happening throughout all the bending, feeding and rotation operations, the G-code is ready to be used in the bending machine system through FlashCut’s CNC software.

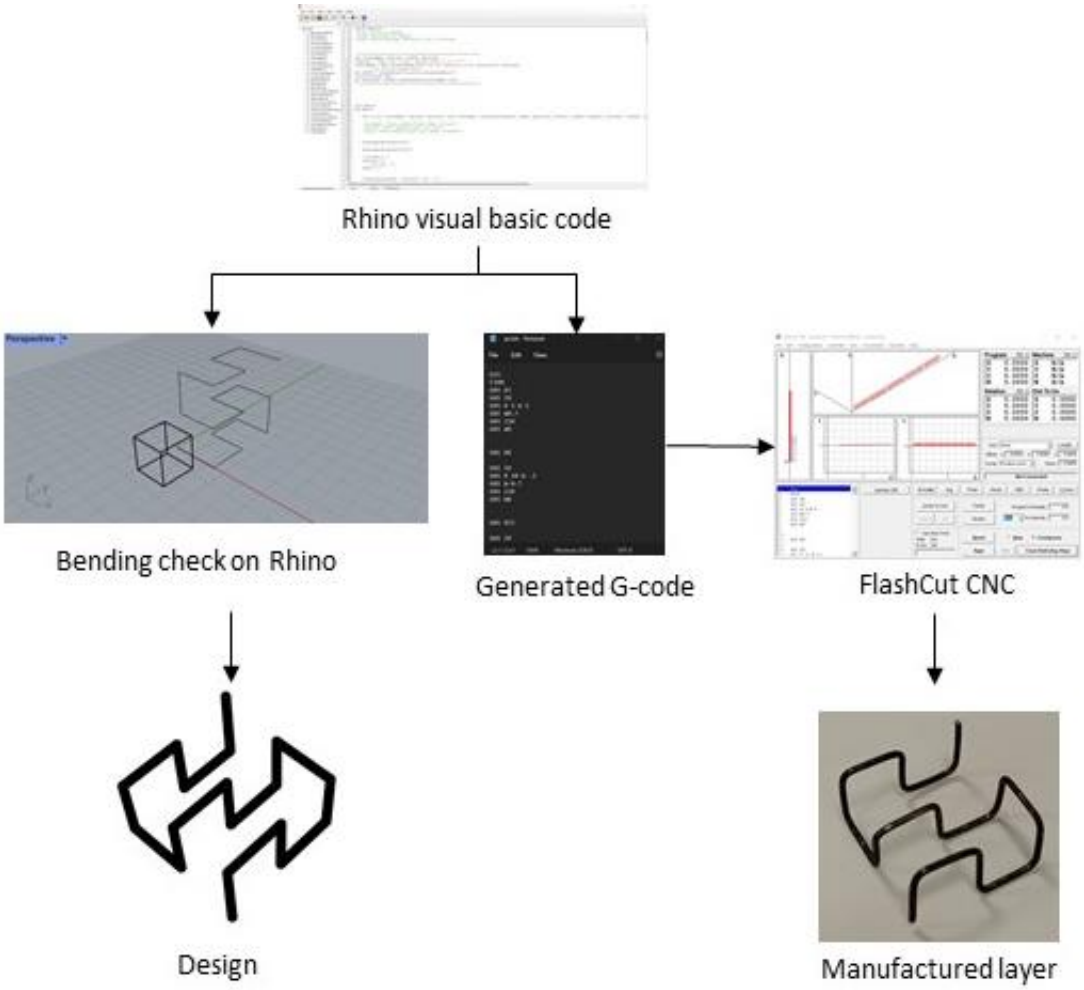

Figure 3-19: Process flow and simulation using Rhino and FlashCut CNC.

For one operation in the machine, a set of G-Codes need to be engaged. For example, one clockwise bending operation (e.g., B_{90}) needs to follow the following instructions one by one:

1 Feeding the straight wire (if no feeding is already done)

2 Engagement of the bending tool

3 Clockwise rotation of the bending tool

4 Counter-clockwise rotation of the bending tool

5 Disengagement of the bending tool

According to the instructions, the G-code looks like this:

1	G01 X8;	Assuming Lx or Ly is 10 mm, 2 mm is fed in the rotation operation
2	G01 Z10;	Z axis moves 0 to 10 mm to engage a straight wire, depending on the calibration
3	G01 W-190 X10;	W is calibrated to each degree of rotation here, and the rotation is 190 degree
4	G01 W-100;	The tool is partially reverted; this helps to disengage the wire from the tool
5	G01 Z0;	Moves the tool to its initial position
6	G01 W0;	Rotates the tool to its initial position

Because of the character of the bending tool, the X feed in line 3 and the partial revert position of the tool in line 4 is essential to have a smooth bending operation. Without proper disengaging, the tool tends to pull off the wire, hence destroying the part.

3.4 Proposed lattice designs that are fabricable using the proposed bending machine

3.4.1 Fabrication process for body centered cubic (BCC) structure

BCC has a strut node connectivity of Z = 8. To achieve this a single unit cell requires four out-of-phase triangular shapes, which are stacked one over another in a specific way shown in Figure 3-20. First, a design of the phase-shifted layers is simulated (Figure 3-20 (a)) in Rhino, and G-code is generated. The bending machine is used to make the four separate but similar structures like Figure 3-20(b). Two of them are stacked over each other where they have a 90-degree angle in the x-y plane between them. Another set of two is stacked in a similar way and turned over upside down to have the middle nodes align with each other (Figure 3-20(d) and (e)). In Figure 3-20, four unit cells are constructed by stacking four phase-shifted fabricable triangular wire parts.

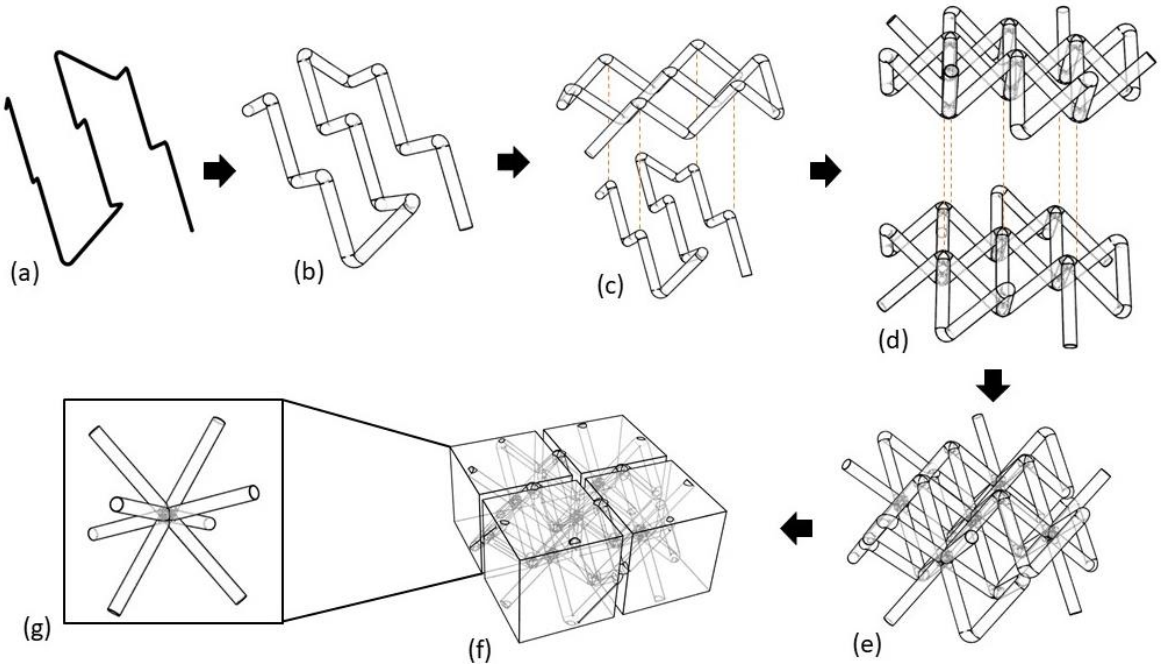

Figure 3-20: Construction of BCC structure using stackable and fabricable Eulerian wire: (a) fabricable design, (b) after bending, (c) first degree stacking of two layers, (d) first degree stacking of two sets of layers, (e) BCC structure, (f) four unit cells constructed from the process, (g) BCC unit cell.

3.4.2 Fabrication Process for the primitive cubic structure

The cubic structure has a strut node connectivity of Z = 6, which can be achieved by using square unit layer lattices stacked following first and second-degree stacking. Two unit layers construct a structure with nodal connections in parallel planes. Transverse missing struts can be filled up with a second-degree stacked unit square lattice shown in Figure 3-21(e). The surface of the cubic lattice can experience missing struts. If the manufactured part has a lot of unit cells, the missing strut percentage will go down, as they occur only at the surface layer.

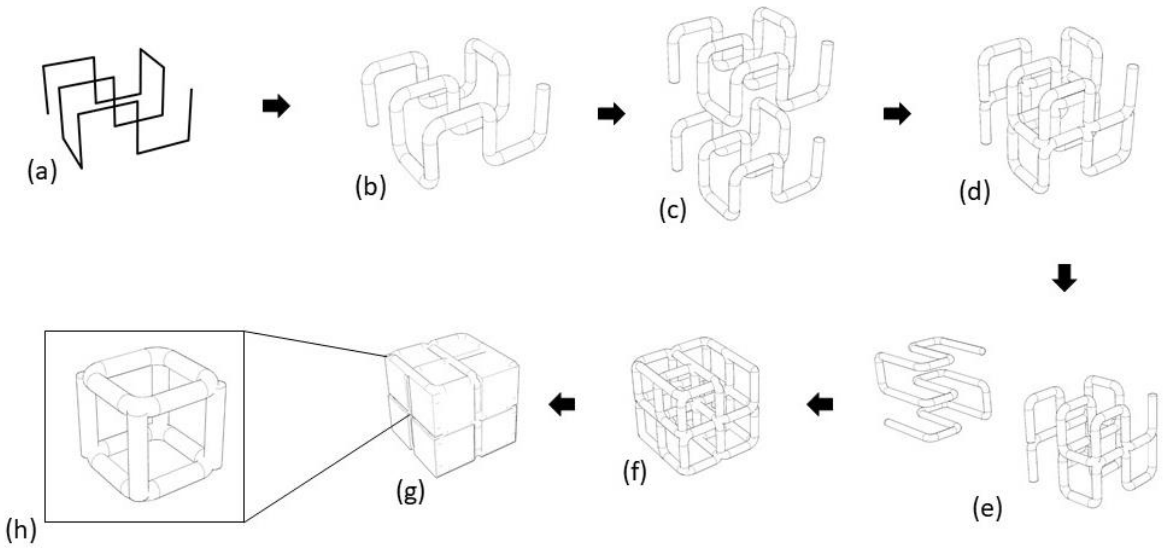

Figure 3-21: Construction of cubic structure using stackable and fabricable Eulerian wire: (a) fabricable design, (b) after bending, (c) first degree stacking of two layers, (d) after stacking two layers, (e) second degree stacking of two sets of layers, (f) primitive cubic structure, (g) eight unit cells constructed from the process, (h) cubic unit cell.

3.4.3 Fabrication process for primitive cubic structure allowing manual bending

A cubic lattice can also be manufactured using a continuous rod [10], [23]. To have a structure like this, manual bending is necessary at some points. Figure 3-22 (a, b) show the design and manual bending points for the construction of a metal lattice. This design can also suffer missing struts at the surface like the previous cubic lattice design.

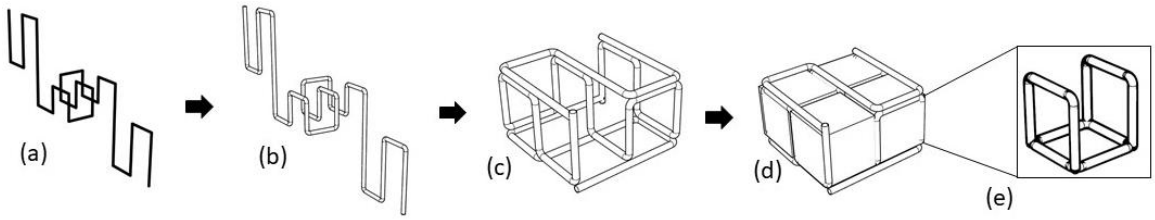

Figure 3-22: Construction of cubic structure using stackable and fabricable continuous Eulerian wire: (a) fabricable design, (b) after bending, (c) after manual bending, (d) four unit cells constructed from the process, (e) cubic unit cell from manual bending.

3.4.4 Fabrication process for octet structure

Octet structures are more complicated than the previous structures. It has a strut node connectivity, Z = 12. The shape of a unit octet is shown in Figure 3-23 (f). An octet structure has similar connectivity as both FCC and BCC. In other words, FCC and BCC are subsets of the octet structure. Therefore, more layers can be stacked in pre-constructed BCC and FCC structures to get an octet structure. Figure 3-23 shows how an octet structure can be constructed from a pre-constructed BCC structure. After building a BCC structure (Figure 3-23(a)), a layer is taken for reference. Phase shifted triangular structures are stacked horizontally to get the horizontal strut node connections available in octet, hence doing a second-degree stacking.

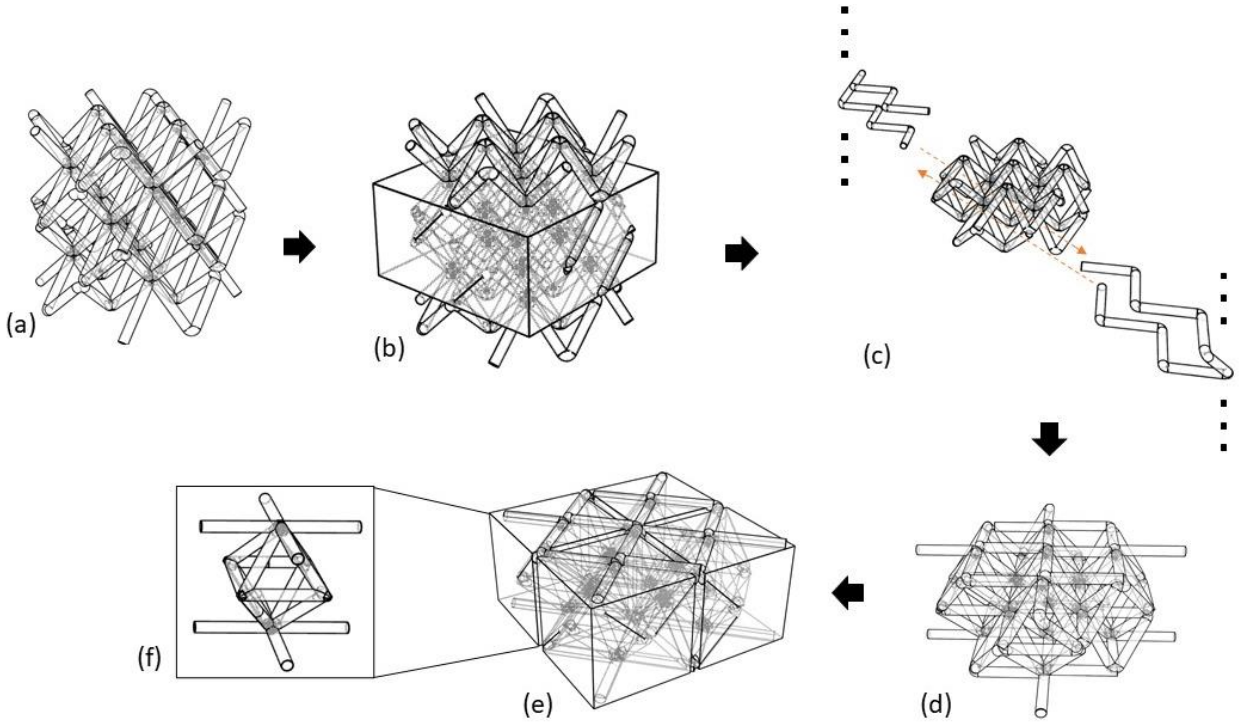

Figure 3-23: Construction of octet structure using stackable and fabricable Eulerian wire: (a) preconstructed BCC, (b) one layer taken for making octet, (c) second degree stacking, (d) octet single layer, (e) four octet unit cell constructed from the process, (f) octet unit cell.

3.5 Loose lattice joining method

After generating a loose lattice structure, the unjointed nodes need to be joined by a convenient metal joining method. If the unit cell size of the lattice structure is small and the geometry is complex, the traditional metal joining methods would not be a good solution. Joining methods like soldering and arc or other types of welding will not be reachable to some particular nodes.

One way of joining the nodes would be dipping the loose structure into a liquid carrier system (LCS) which delivers adhesive material to the nodes. Previously, studies have been done to find effective joining methods for loose lattices [71], [72]. One way would be polymer-metal adhesive bonding by using epoxy as LCS, and the other way would be transient liquid phase (TLP) diffusion

bonding, where the LCS is made of a solvent, a binder, and inorganic particles which need to be transferred to the nodes. In a vacuum furnace with high temperature, the inorganic particles transferred to the nodes will diffuse to the base metal, hence joining the nodes of the loose structure.

In this research, TLP diffusion bonding was investigated as a potential method of joining the loose lattice. TLP bonding is used as a metal-metal joining method that has both diffusion and brazing characteristics. In this method, metal/alloy particles are delivered in between the two to-be-connected surfaces of the base material used in the loose lattice. The base material used for loose lattice is AISI 1006 low carbon steel, and Nicrobraz 51 powder was taken as the inorganic metal particle, which is to be transferred to the nodes for diffusion. As a binder polymer, Polymethyl methacrylate (PMMA) was chosen. This amorphous thermoplastic material has a sufficient gap-filling quality, which is essential for node joining. Its low density ($\sim 1.17\ \mathrm{gm/cm^3}$), relatively high flash point(>250˚C), and good tensile strength (72 MPa) make it perfect for this purpose. As a solvent, 1,3 Dioxolane was considered as it has a quick evaporation rate, low density ($\sim 1.06\ \mathrm{gm/cm^3}$) with very low toxicity. The solute and solvent were stirred with a magnetic stirrer for about 8 hours before mixing the inorganic particles (Nicrobraz powder). The Nicrobraz powder was added to the solution with a 45% (v/v) ratio. These concentrations for binder, solvent, and inorganic particles were optimized by Khoda et al. [71]. As the inorganic metal powder has a different density than the solution, sedimentation occurs if the suspension is kept still. Before dipping the loose structure, the suspension was stirred using a magnetic stirrer, and the loose structure was dipped. The dipping method is elaborately discussed in Chapter four.

If the dipped loose lattice is kept at a high temperature, the interlayer alloy (Nicrobraz powder) will melt and join the interlayers by capillary action. A liquid bridge connects between the two-

joining surfaces, and local diffusion happens between the interlayer alloy and the base metal, which ultimately joins the nodes. A furnace by Desktop Metal was used in this study. The temperature profile is shown in Figure 3-24. The temperature goes over 500˚C after about 17 hours, which is over the evaporation temperature of the binder PMMA. After about 21 hours, the temperature goes over 1200˚C, which ensures the diffusion process. After achieving the highest temperature, the part is cooled down for over 35 hours to have the least amount of residual stress in the part. Figure 3-25 shows some of the constructed lattices by joining soldering for proof of concept and by joining using TLP process.

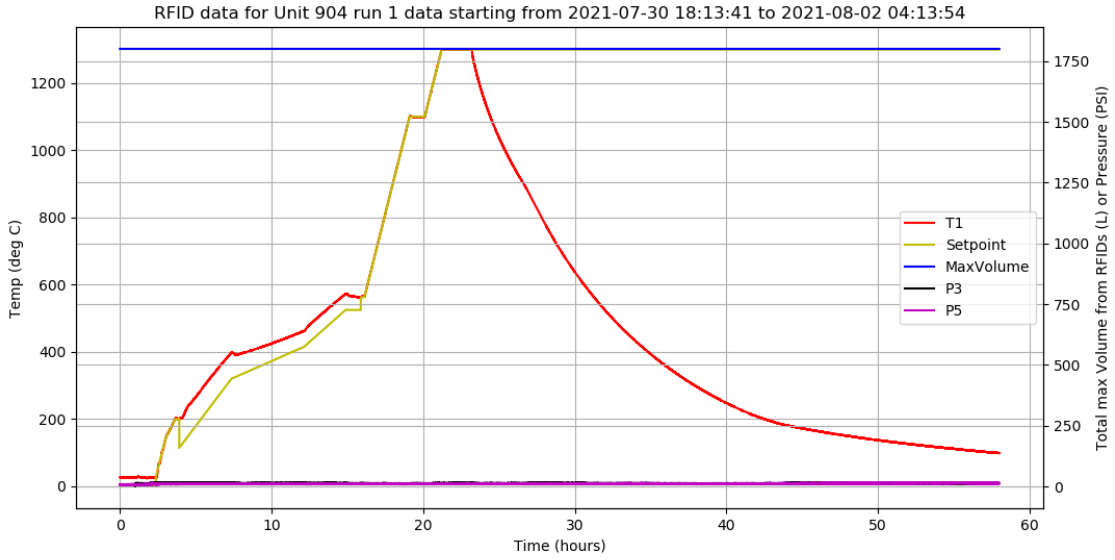

Figure 3-24: Temperature profile obtained from experiment in furnace (Desktop Metal)

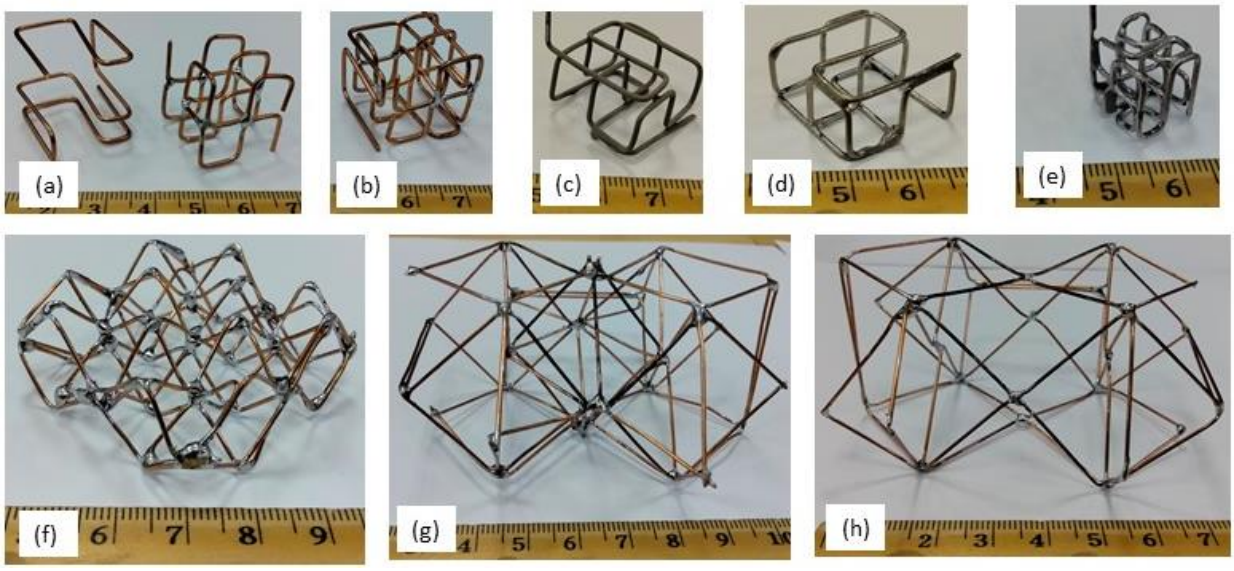

Figure 3-25: Manufactured lattice structures, (a,b) Primitive cubic lattice by second degree stacking (copper wire with solder joining), cubic lattice from continuous rod (c) after dipping, (d) after joining, (e) higher cell size(2×2×2) (AISI 1006 metal with TLP joining), (f) BCC, (g) octet, (h) FCC lattice manufactured by proposed process (Copper wire with solder joining).

CHAPTER 4 : CONCLUSIONS

In this study, two new types of manufacturing lattices with two different materials (polymer and metal) are proposed and discussed. For polymer lattice manufacturing, it is found that filament deposition direction has an effect on polymer lattice manufacturing, and it can be minimized by utilizing assembled parts following Eulerian paths for continuity in filament deposition. Continuity in filament deposition changes the failure mode for both bending and stretch-dominated lattice structures and makes them suitable for applications that require energy absorption. A low relative density was also achievable by the assembly method, and even less density is achievable by design, where the direct print is restricted by the parameters of the manufacturing process. As the assembly method does not incorporate support materials, a lot of manufacturing options open up, which are unachievable by direct print, e. g. strut angle variation, very low density, and complicated porosity without material entrapment.

For the range of relative density tested for cubic and octet structures (5.46% – 16.3%) generally the relative strength is found higher in assembly-based structures. In cubic structure, middle base plate did not show any load bearing behavior, where octets' middle base plate showed significant deformation. Direct print and assembled cubic structures showed significant difference in failure, while failure for octet for both type was almost the same. These can be attributed by the difference in printing process of direct and assembled based structures. In conclusion, assembly based lattices can be a potential candidate for all lightweight applications. As future work other designs for lattices like BCC, FCC, cuboct etc. can be done and tested. These characteristics of different lattices can be useful in selecting the assemble based design for various applications.

A novel way of manufacturing metal lattice was also studied, the challenges of bending a 3D structure from a machine are acknowledged, and some way of overcoming this obstacle of wire hitting itself is discussed. Some new ideas for manufacturing wire metal lattices are presented, and some possibilities of periodic and aperiodic cubic, BCC, FCC, and octet lattices are introduced. For the joining of the loose lattice manufactured by this process, Transient liquid phase (TLP) diffusion bonding is proposed and studied. From the study it can be concluded that this new metal lattice fabrication process has potential to be used as a regular metal lattice manufacturing process. As future work aperiodic metal lattice manufacturing process can be studied. As the dimension can be programable through an automatic process, presented lattice manufacturing process can be used in quick fabrication of topologically optimized metal structures. The versatility of the fabricable designs can facilitate the manufacturing of auxetic materials using wire bending process.

REFERENCES

[1] B. Khoda, A. M. M. N. Ahsan, A. N. Shovon, and A. I. Alam, "3D metal lattice structure manufacturing with continuous rods," *Scientific Reports*, vol. 11, no. 1, p. 434, 2021, doi: 10.1038/s41598-020-79826-6.

[2] D. J. Brackett, I. A. Ashcroft, R. D. Wildman, and R. J. M. Hague, "An error diffusion based method to generate functionally graded cellular structures," *Computers & Structures*, vol. 138, pp. 102–111, 2014, doi: https://doi.org/10.1016/j.compstruc.2014.03.004.

[3] J. C. Maxwell, "L. On the calculation of the equilibrium and stiffness of frames," *The London, Edinburgh, and Dublin Philosophical Magazine and Journal of Science*, vol. 27, no. 182, pp. 294–299, 1864, doi: 10.1080/14786446408643668.

[4] H. N. G. Wadley, K. P. Dharmasena, M. R. O'Masta, and J. J. Wetzel, "Impact response of aluminum corrugated core sandwich panels," *International Journal of Impact Engineering*, vol. 62, pp. 114–128, 2013, doi: http://dx.doi.org/10.1016/j.ijimpeng.2013.06.005.

[5] M. G. Rashed, M. Ashraf, R. A. W. Mines, and P. J. Hazell, "Metallic microlattice materials: A current state of the art on manufacturing, mechanical properties and applications," *Materials & Design*, vol. 95, pp. 518–533, 2016, doi: http://dx.doi.org/10.1016/j.matdes.2016.01.146.

[6] T. A. Schaedler and W. B. Carter, "Architected Cellular Materials," *Annual Review of Materials Research*, vol. 46, no. 1, pp. 187–210, 2016, doi: 10.1146/annurev-matsci-070115-031624.

[7] C. C. Seepersad, J. K. Allen, D. L. McDowell, and F. Mistree, "Multifunctional Topology Design of Cellular Material Structures," *Journal of Mechanical Design*, vol. 130, no. 3, pp. 031404-031404–13, 2008, doi: 10.1115/1.2829876.

[8] A. G. Evans, J. W. Hutchinson, N. A. Fleck, M. F. Ashby, and H. N. G. Wadley, "The topological design of multifunctional cellular metals," *Progress in Materials Science*, vol. 46, no. 3, pp. 309–327, 2001, doi: http://dx.doi.org/10.1016/S0079-6425(00)00016-5.

[9] H. D. Carlton *et al.*, "Mapping local deformation behavior in single cell metal lattice structures," *Acta Materialia*, 2017, doi: 10.1016/j.actamat.2017.02.023.

[10] B. Khoda and A. M. M. N. Ahsan, "A Novel Rapid Manufacturing Process for Metal Lattice Structure," *3D Printing and Additive Manufacturing*, 2021, doi: 10.1089/3dp.2020.0184.

[11] C. C. Seepersad, J. K. Allen, D. L. McDowell, and F. Mistree, “Robust Design of Cellular Materials With Topological and Dimensional Imperfections,” *Journal of Mechanical Design*, vol. 128, no. 6, pp. 1285–1297, 2006, doi: 10.1115/1.2338575.

[12] A.-J. Wang and D. L. McDowell, “Effects of defects on in-plane properties of periodic metal honeycombs,” *International Journal of Mechanical Sciences*, vol. 45, no. 11, pp. 1799–1813, 2003, doi: https://doi.org/10.1016/j.ijmecsci.2003.12.007.

[13] W. Yuan, H. Song, L. Lu, and C. Huang, “Effect of local damages on the buckling behaviour of pyramidal truss core sandwich panels,” *Composite Structures*, vol. 149, pp. 271–278, 2016, doi: https://doi.org/10.1016/j.compstruct.2016.04.031.

[14] T. A. Schaedler *et al.*, “Ultralight metallic microlattices,” *Science (1979)*, vol. 334, no. 6058, 2011, doi: 10.1126/science.1211649.

[15] M. Yetna N’Jock *et al.*, “Characterization of 100Cr6 lattice structures produced by robocasting,” *Materials and Design*, 2017, doi: 10.1016/j.matdes.2017.02.066.

[16] C. Sennewald *et al.*, “Metal sandwiches and metal-matrix-composites based on 3D woven wire structures for hybrid lightweight construction,” *Advanced Engineering Materials*, vol. 16, no. 10, 2014, doi: 10.1002/adem.201400180.

[17] D. T. Queheillalt and H. N. G. Wadley, “Titanium alloy lattice truss structures,” *Materials and Design*, vol. 30, no. 6, 2009, doi: 10.1016/j.matdes.2008.09.015.

[18] J. Mun, B. G. Yun, J. Ju, and B. M. Chang, “Indirect additive manufacturing based casting of a periodic 3D cellular metal - Flow simulation of molten aluminum alloy,” *Journal of Manufacturing Processes*, vol. 17, 2015, doi: 10.1016/j.jmapro.2014.11.001.

[19] S. Das, D. L. Bourell, and S. S. Babu, “Metallic materials for 3D printing,” *MRS Bulletin*, vol. 41, no. 10. 2016. doi: 10.1557/mrs.2016.217.

[20] B. Lozanovski *et al.*, “Computational modelling of strut defects in SLM manufactured lattice structures,” *Materials and Design*, 2019, doi: 10.1016/j.matdes.2019.107671.

[21] M. Bici *et al.*, “Development of a multifunctional panel for aerospace use through SLM additive manufacturing,” 2018. doi: 10.1016/j.procir.2017.12.202.

[22] H. ZHOU *et al.*, “Lightweight structure of a phase-change thermal controller based on lattice cells manufactured by SLM,” *Chinese Journal of Aeronautics*, 2019, doi: 10.1016/j.cja.2018.08.017.

[23] B. Khoda, A. M. M. Ahsan, A. N. Shovon, and A. I. Alam, “3D metal lattice structure manufacturing with continuous rods,” *Scientific Reports*, vol. 11, no. 1, pp. 1–17, 2021.

[24] S. R. Rajpurohit and H. K. Dave, “Effect of process parameters on tensile strength of FDM printed PLA part,” *Rapid Prototyping Journal*, 2018.

[25] S. T. Lee, L. Kareko, and J. Jun, “Study of thermoplastic PLA foam extrusion,” *Journal of Cellular Plastics*, 2008, doi: 10.1177/0021955X08088859.

[26] A. M. M. N. Ahsan, M. A. Habib, and B. Khoda, “Resource based process planning for additive manufacturing,” *Computer-Aided Design*, vol. 69, pp. 112–125, 2015, doi: https://doi.org/10.1016/j.cad.2015.03.006.

[27] N. Ahsan and B. Khoda, “AM optimization framework for part and process attributes through geometric analysis,” *Additive Manufacturing*, vol. 11, pp. 85–96, 2016, doi: http://dx.doi.org/10.1016/j.addma.2016.05.013.

[28] A. Habib and B. Khoda, “Attribute driven process architecture for additive manufacturing.” 2016.

[29] A. K. M. Khoda, I. T. Ozbolat, and B. Koc, “A functionally gradient variational porosity architecture for hollowed scaffolds fabrication,” *Biofabrication*, vol. 3, no. 3, 2011, doi: 10.1088/1758-5082/3/3/034106.

[30] R. Gautam, S. Idapalapati, and S. Feih, “Printing and characterisation of Kagome lattice structures by fused deposition modelling,” *Materials & Design*, vol. 137, pp. 266–275, 2018, doi: https://doi.org/10.1016/j.matdes.2017.10.022.

[31] A. Nazir, K. M. Abate, A. Kumar, and J.-Y. Jeng, “A state-of-the-art review on types, design, optimization, and additive manufacturing of cellular structures,” *The International Journal of Advanced Manufacturing Technology*, vol. 104, no. 9, pp. 3489–3510, 2019, doi: 10.1007/s00170-019-04085-3.

[32] G. Dong, G. Wijaya, Y. Tang, and Y. F. Zhao, “Optimizing process parameters of fused deposition modeling by Taguchi method for the fabrication of lattice structures,” *Additive Manufacturing*, vol. 19, pp. 62–72, 2018.

[33] L. Azzouz *et al.*, “Mechanical properties of 3-D printed truss-like lattice biopolymer non-stochastic structures for sandwich panels with natural fibre composite skins,” *Composite Structures*, vol. 213, pp. 220–230, 2019, doi: https://doi.org/10.1016/j.compstruct.2019.01.103.

[34] S. Bhandari, R. A. Lopez-Anido, and D. J. Gardner, “Enhancing the interlayer tensile strength of 3D printed short carbon fiber reinforced PETG and PLA composites via annealing,” *Additive Manufacturing*, vol. 30, p. 100922, 2019, doi: https://doi.org/10.1016/j.addma.2019.100922.

[35] P. Jiang, E. C. de Meter, and S. Basu, “The influence of defects on the elastic response of lattice structures resulting from additive manufacturing,” *Computational Materials Science*, vol. 199, p. 110716, 2021, doi: https://doi.org/10.1016/j.commatsci.2021.110716.

[36] J. Kiendl and C. Gao, “Controlling toughness and strength of FDM 3D-printed PLA components through the raster layup,” *Composites Part B: Engineering*, vol. 180, p. 107562, 2020.

[37] H. J. Rathbun *et al.*, “Measurement and simulation of the performance of a lightweight metallic sandwich structure with a tetrahedral truss core,” *Journal of Applied Mechanics, Transactions ASME*, vol. 71, no. 3, 2004, doi: 10.1115/1.1757487.

[38] V. I. Voloshin, *Introduction to graph theory*. 2009. doi: 10.2307/2319240.

[39] L. Dong, V. Deshpande, and H. Wadley, “Mechanical response of Ti–6Al–4V octet-truss lattice structures,” *International Journal of Solids and Structures*, vol. 60–61, pp. 107–124, 2015, doi: https://doi.org/10.1016/j.ijsolstr.2015.02.020.

[40] R. N. Glaesener, E. A. Träff, B. Telgen, R. M. Canonica, and D. M. Kochmann, “Continuum representation of nonlinear three-dimensional periodic truss networks by on-the-fly homogenization,” *International Journal of Solids and Structures*, vol. 206, 2020, doi: 10.1016/j.ijsolstr.2020.08.013.

[41] W. Liu, H. Song, Z. Wang, J. Wang, and C. Huang, “Improving mechanical performance of fused deposition modeling lattice structures by a snap-fitting method,” *Materials & Design*, vol. 181, p. 108065, 2019, doi: https://doi.org/10.1016/j.matdes.2019.108065.

[42] V. S. Deshpande, N. A. Fleck, and M. F. Ashby, “Effective properties of the octet-truss lattice material,” *Journal of the Mechanics and Physics of Solids*, vol. 49, no. 8, pp. 1747–1769, 2001, doi: https://doi.org/10.1016/S0022-5096(01)00010-2.

[43] L. J. Gibson and M. F. Ashby, *Cellular Solids: Structure and Properties*, 2nd ed. Cambridge: Cambridge University Press, 1997. doi: DOI: 10.1017/CBO9781139878326.

[44] W. Chen, Z. Liu, H. M. Robinson, and J. Schroers, “Flaw tolerance vs. performance: A tradeoff in metallic glass cellular structures,” *Acta Materialia*, vol. 73, pp. 259–274, 2014, doi: https://doi.org/10.1016/j.actamat.2014.04.026.

[45] C. Li *et al.*, “Architecture design of periodic truss-lattice cells for additive manufacturing,” *Additive Manufacturing*, vol. 34, p. 101172, 2020, doi: https://doi.org/10.1016/j.addma.2020.101172.

[46] M. F. Ashby, “The properties of foams and lattices,” *Philos Trans A Math Phys Eng Sci*, vol. 364, no. 1838, pp. 15–30, 2006, doi: 10.1098/rsta.2005.1678.

[47] J. C. Maxwell, “On the Calculation of the Equilibrium and Stiffness of Frames,” *Philosophical Magazine*, vol. 27, p. 294, 1864.

[48] W. Chen, S. Watts, J. A. Jackson, W. L. Smith, D. A. Tortorelli, and C. M. Spadaccini, “Stiff isotropic lattices beyond the Maxwell criterion,” *Science Advances*, vol. 5, no. 9, p. eaaw1937, 2019, doi: 10.1126/sciadv.aaw1937.

[49] I. Maskery *et al.*, “Insights into the mechanical properties of several triply periodic minimal surface lattice structures made by polymer additive manufacturing,” *Polymer (Guildf)*, vol. 152, 2018, doi: 10.1016/j.polymer.2017.11.049.

[50] D. K. Mishra and P. M. Pandey, “Experimental investigation into the fabrication of green body developed by micro-extrusion-based 3D printing process,” *Polymer Composites*, 2020, doi: 10.1002/pc.25514.

[51] K. Yang, J. Wang, L. Jia, G. Yang, H. Tang, and Y. Li, “Additive manufacturing of Ti-6Al-4V lattice structures with high structural integrity under large compressive deformation,” *Journal of Materials Science and Technology*, 2019, doi: 10.1016/j.jmst.2018.10.029.

[52] L. Yang, O. Harrysson, D. Cormier, H. West, H. Gong, and B. Stucker, “Additive Manufacturing of Metal Cellular Structures: Design and Fabrication,” *JOM*. 2015. doi: 10.1007/s11837-015-1322-y.

[53] D. K. Mishra and P. M. Pandey, “Mechanical behaviour of 3D printed ordered pore topological iron scaffold,” *Materials Science and Engineering A*, 2020, doi: 10.1016/j.msea.2020.139293.

[54] K. Cooper, P. Steele, B. Cheng, and K. Chou, “Contact-free support structures for part overhangs in powder-bed metal additive manufacturing,” *Inventions*, 2018, doi: 10.3390/inventions3010002.

[55] M. Dallago, S. Raghavendra, V. Luchin, G. Zappini, D. Pasini, and M. Benedetti, “Geometric assessment of lattice materials built via Selective Laser Melting,” in *Materials Today: Proceedings*, 2019, vol. 7. doi: 10.1016/j.matpr.2018.11.096.

[56] X. Han, H. Zhu, X. Nie, G. Wang, and X. Zeng, “Investigation on selective laser melting AlSi10Mg cellular lattice strut: Molten pool morphology, surface roughness and dimensional accuracy,” *Materials*, vol. 11, no. 3, 2018, doi: 10.3390/ma11030392.

[57] K. C. Cheung and N. Gershenfeld, “Reversibly assembled cellular composite materials,” *Science (1979)*, 2013, doi: 10.1126/science.1240889.

[58] S. Jiang, F. Sun, X. Zhang, and H. Fan, “Interlocking orthogrid: An efficient way to construct lightweight lattice-core sandwich composite structure,” *Composite Structures*, vol. 176, 2017, doi: 10.1016/j.compstruct.2017.05.029.

[59] E. Miguel, M. Lepoutre, and B. Bickel, “Computational design of stable planar-rod structures,” in *ACM Transactions on Graphics*, 2016, vol. 35, no. 4. doi: 10.1145/2897824.2925978.

[60] D. J. Sypeck and H. N. G. Wadley, “Multifunctional microtruss laminates: Textile synthesis and properties,” *Journal of Materials Research*, vol. 16, no. 3, 2001, doi: 10.1557/JMR.2001.0117.

[61] A. Gilbert, “An in-office wire-bending robot for lingual orthodontics.,” *J Clin Orthod*, 2011.

[62] Z. Xia, H. Deng, S. Weng, Y. Gan, J. Xiong, and H. Wang, “Development of a robotic system for orthodontic archwire bending,” 2016. doi: 10.1109/ICRA.2016.7487200.

[63] J. Mah and R. Sachdeva, “Computer-assisted orthodontic treatment: the SureSmile process,” *Am J Orthod Dentofacial Orthop*, 2001, doi: 10.1067/mod.2001.117686.

[64] J. Jin-gang, P. Bo, Z. Yong-de, W. Zhao, L. Yi, and W. Fu-jia, “Structural Analysis and dynamics Simulation of Orthodontic Archwire Bending Robot,” *International Journal of Control and Automation*, 2015, doi: 10.14257/ijca.2015.8.9.20.

[65] R. A. Hamid and T. Ito, “Integration of CAD/CAM in developing the CNC dental wire bending machine,” in *Journal of Advanced Mechanical Design, Systems and Manufacturing*, 2018, vol. 12, no. 3. doi: 10.1299/jamdsm.2018jamdsm0079.

[66] Y. C. Chang and R. H. Crawford, “Design of a desktop wire-feed prototyping machine,” 2020.

[67] W. Z. -, “Research of 3D Virtual Design and Automated Bending of Oral Orthodontic Archwire,” *International Journal of Advancements in Computing Technology*, vol. 5, no. 8, 2013, doi: 10.4156/ijact.vol5.issue8.84.

[68] J. Jin-gang, Z. Yong-de, J. Ming-liang, and W. chun-ge, “Bending process analysis and structure design of orthodontic archwire bending robot,” *International Journal of Smart Home*, vol. 7, no. 5, 2013, doi: 10.14257/ijsh.2013.7.5.33.

[69] H. Xu, E. Knoop, S. Coros, and M. Bächer, “Bend-it,” *ACM Transactions on Graphics*, 2018, doi: 10.1145/3272127.3275089.

[70] W. Lira, C. W. Fu, and H. Zhang, “Fabricable eulerian wires for 3D shape abstraction,” 2018. doi: 10.1145/3272127.3275049.

[71] B. Khoda, A. M. M. N. Ahsan, A. N. Shovon, and A. I. Alam, “3D metal lattice structure manufacturing with continuous rods,” *Scientific Reports*, vol. 11, no. 1, p. 434, 2021, doi: 10.1038/s41598-020-79826-6.

[72] B. Khoda and A. M. M. N. Ahsan, “A Novel Rapid Manufacturing Process for Metal Lattice Structure,” *3D Printing and Additive Manufacturing*, 2021, doi: 10.1089/3dp.2020.0184.

BIBLIOGRAPHY OF THE AUTHOR

Adeeb Ibne Alam was born in Mymensingh, Bangladesh on February 6, 1994. He completed his bachelor's degree in Mechanical Engineering from Bangladesh University of Engineering and Technology (BUET) in February 2017. He started his MS in Mechanical Engineering in Fall 2019 at the University of Maine with Dr. Bashir Khoda.

Adeeb is a candidate for the Master of Science in Mechanical Engineering from the University of Maine in August 2022.